Article:

Villar Martín, M., Castro-Rodríguez, N., Pereira Santaella, M. et al. (2023) Limited impact of jet-induced feedback in the multi-phase nuclear interstellar medium of 4C12.50. Astronomy & Astrophysics, 673. A25. ISSN: 0004-6361

https://doi.org/10.1051/0004-6361/202245418

A&A 673, A25 (2023)
https://doi.org/10.1051/0004-6361/202245418
© The Authors 2023

Astronomy & Astrophysics

Limited impact of jet-induced feedback in the multi-phase nuclear interstellar medium of 4C12.50

M. Villar Martín[1], N. Castro-Rodríguez[2,3], M. Pereira Santaella[4], I. Lamperti[1], C. Tadhunter[5], B. Emonts[6], L. Colina[1], A. Alonso Herrero[7], A. Cabrera-Lavers[2,3], and E. Bellocchi[8,9]

[1] Centro de Astrobiología (CAB), CSIC-INTA, Ctra. de Ajalvir, km 4, 28850 Torrejón de Ardoz, Madrid, Spain
e-mail: `villarmm@cab.inta-csic.es`
[2] GRANTECAN, Cuesta de San José s/n, 38712 Breña Baja, La Palma, Spain
[3] Instituto de Astrofísica de Canarias, Vía Láctea s/n, 38200 La Laguna, Tenerife, Spain
[4] Observatorio Astronómico Nacional (OAN-IGN) – Observatorio de Madrid, Alfonso XII, 3, 28014 Madrid, Spain
[5] Department of Physics & Astronomy, The Hicks Building, University of Sheffield, Hounsfield Road, Sheffield S3 7RH, UK
[6] National Radio Astronomy Observatory, 520 Edgemont Road, Charlottesville, VA 22903, USA
[7] Centro de Astrobiología (CAB), CSIC-INTA, Camino Bajo del Castillo s/n, 28692 Villanueva de la Cañada, Madrid, Spain
[8] Departamento de Física de la Tierra y Astrofísica, Fac. de CC Físicas, Universidad Complutense de Madrid, Plaza Ciencias 1, 28040 Madrid, Spain
[9] Instituto de Física de Partículas y del Cosmos IPARCOS, Fac. CC Físicas, Universidad Complutense de Madrid, Plaza Ciencias 1, 28040 Madrid, Spain

Received 9 November 2022 / Accepted 24 February 2023

ABSTRACT

Context. 4C12.50 (IRAS 13451+1232) at $z = 0.122$ is an ultraluminous infared radio galaxy that has often been proposed as a prime candidate for the link between ultraluminous infared galaxies and young radio galaxies. It is also an interesting target to investigate whether and how radio-induced feedback affects the evolution of galaxies in the early phases of radio activity.
Aims. We study, in detail for the first time, the hot (≥1500 K) molecular gas in 4C12.50. The potential impact of the radio jet on this gas phase, as well as on the star formation activity, are investigated. We also study the ionised (including coronal) gas as traced by the near-infrared lines.
Methods. Using near-infrared long slit spectroscopy obtained with EMIR on GTC and X-shooter on VLT, we analyse the emission line spectrum of the ionised, coronal, and, specially, the hot molecular gas in the western nucleus hosting the compact radio jet. Based on high spatial resolution ALMA CO(2–1) data, we also revise the location of 4C12.50 in the Kennicutt-Schmidt diagram in order to investigate whether star formation is suppressed.
Results. 4C12.50 hosts $(2.1 \pm 0.4) \times 10^4\ M_\odot$ of hot molecular gas. An unusually high rotational temperature $T_{\rm rot} = 3020 \pm 160$ K is inferred. The molecular gas mass obeys a power-law temperature distribution, $\frac{{\rm d}M_{\rm H2}}{{\rm d}T} \propto T^{-5}$, from $T \sim 300$ K and up to ∼3000 K. Both results support the idea that shocks (probably induced by the radio jet) contribute to the heating and excitation of the hot molecular gas. A molecular outflow is not detected. The coupling of the outflowing ionised and neutral outflows with the hot molecular gas is poor. Contrary to other studies, we claim that there is no evidence for star formation suppression in this object.
Conclusions. If radio-induced feedback can regulate the star formation activity in galaxies, 4C12.50 is a promising candidate to reveal this phenomenon in action. However, we find no solid evidence for a current or past impact of this mechanism on the evolution of this system, neither by clearing out the dusty central cocoon efficiently, nor by suppressing the star formation activity.

Key words. galaxies: active – galaxies: individual: 4C12.50 – ISM: jets and outflows – galaxies: evolution

1. Introduction

Gigahertz-peaked spectrum (GPS) sources are compact and often powerful radio sources. They are estimated to make up around 10% of the bright radio-source population (O'Dea 1998; O'Dea & Saikia 2021, Sadler 2016). There are three main hypotheses as to their nature, which can vary from source to source. They might be: (1) very young radio galaxies which will evolve into large radio galaxies; (2) compact due to the confinement by interactions with dense gas in their environments; or (3) transient or intermittent sources (O'Dea & Saikia 2021).

The GPS sources are entirely contained within the extent of the narrow-line region (NLR, ≲1 kpc). Because of the similar spatial scales, the feedback effects that result from the interaction between the radio source and the dense circumnuclear interstellar medium (ISM) can be very strong. Thus, they are interesting targets to investigate whether and how radio-induced feedback affects the evolution of galaxies in the early phases of radio activity (O'Dea 1998; Holt et al. 2003, 2011; Morganti et al. 2013; Santoro et al. 2020).

4C12.50 (IRAS 13451+1232) at $z = 0.122$ (luminosity distance $D_{\rm L} = 573$ Mpc) is one of the closest and best known GPS sources ($P_{5\,\rm GHz} \sim 10^{33}$ W Hz^{-1}; O'Dea 1998; Holt et al. 2003). Radio emission stretching outside the host galaxy provides evidence of a previous radio outburst that occured $\sim 10^{7-8}$ yr ago (Stanghellini et al. 2005). The jet may have restarted only recently ($<10^5$ yr) after a long period of inactivity or it may be a central component in a continuous supply of energy from the core to the extended lobes (Lister et al. 2003; O'Dea et al. 2000; Stanghellini et al. 2005; Morganti et al. 2013). Jet frustration appears to be working at some level, but the amount of mass seems to be insufficient to confine the jet completely (Morganti et al. 2004, 2013).

4C12.50 has often been suggested to be a prime candidate for the link between ultraluminous infrared galaxies (ULIRGs) and young radio galaxies (Gilmore & Shaw 1986; Morganti et al. 2003, 2013). It is a ULIRG with $L_{\rm IR} = \log(L_{8-1000\,0\,\mu{\rm m}}/L_\odot) = 12.31$ and a star formation rate (SFR) of $\sim 100\,M_\odot$ yr^{-1} (Mirabel et al. 1989; Rupke et al. 2005; Perna et al. 2021; Pereira-Santaella et al. 2021). 4C12.50 is hosted by an elliptical galaxy with two optical nuclei separated by 1.8″ or 4.0 kpc. Additional morphological signs reveal a major merger event which is in the later stages involving at least one gas-rich galaxy (e.g. Heckman et al. 1986; Emonts et al. 2016). The western, primary nucleus is active and hosts the compact jet. This has a small size (∼220 pc) and twin-jet morphology. (Grandi 1977; Gilmore & Shaw 1986; Veilleux et al. 1997). The high [OIII]λ5007 luminosity $L_{\rm [OIII]} \sim 2.0 \times 10^{42}$ erg s^{-1} (Tadhunter et al. 2011) is in the quasar regime (Zakamska et al. 2003). Therefore, 4C12.50 is a radio-loud type 2 quasar (QSO2).

4C12.50 is very rich in dust and molecular gas with a mass of cold ($\lesssim$25 K) molecular gas $\sim 10^{10}\,M_\odot$ (Dasyra & Combes 2012), in the range of other ULIRGs (Mirabel 1989; Evans et al. 1999; Solomon & Vanden Bout 2005). It is the most molecular gas-rich radio galaxy known in the nearby Universe (e.g. Ocaña Flaquer et al. 2010; Smolčić & Riechers 2011). Most of this gas is highly concentrated within a few kiloparsecs of the western active nucleus, including a small, ∼4-kpc wide disk (Fotopoulou et al. 2019).

This primary nucleus hosts fast outflows (up to ∼2000 km s^{-1}) which have been detected in emission in the ionised phase and in absorption in the cold HI circumnuclear gas (e.g. Holt et al. 2003, 2011; Spoon & Holt 2009, Morganti et al. 2005; Rose et al. 2018; see also Rupke et al. 2005). The ionised and the neutral HI outflows in 4C12.50 are driven by the radio plasma. The compact jet seems to be fighting its way out and emerging from the dense cocoon of gas and dust in the western nucleus, clearing it out via these kinematically extreme outflows (Morganti et al. 2003, 2013).

It is of great interest to investigate the potential impact of this feedback mechanism in the molecular phase, since this is the fuel used by galaxies to form stars. The evidence for a cold molecular outflow in 4C12.50 is controversial. Blueshifted CO(3–2) absorption, (shift relative to the systemic velocity $\Delta V \sim -950$ km s^{-1}), and tentative CO(1–0) absorption, ($\Delta V \sim -1100$ km s^{-1}, Dasyra & Combes 2012), have been reported at a similar velocity as the neutral outflow. On the other hand, posterior studies (some making use of the Atacama Large Millimeter Array, ALMA) could not corroborate this outflow, neither in absorption or emission using different CO lines (Dasyra et al. 2014; Fotopoulou et al. 2019; Lamperti et al. 2022). The detection of outflow signatures in the warm (∼400 K) molecular gas is also controversial. The high-velocity blueshifted mid-infrared (MIR) H_2 emission detected by Dasyra & Combes (2011) could not be confirmed by Guillard et al. (2012).

The outflow imprint is yet to be searched for in the hot (>1500 K) molecular phase. In fact, this gas, which emits the strongest lines in the near-infrared (NIR), has been barely studied in 4C12.50 (Veilleux et al. 1997; Rose et al. 2018). Our goal is to fill this gap in the knowledge of this otherwise widely studied system. We investigate the general hot H_2 properties (mass, temperature, reddening, excitation mechanisms) and whether the outflow has affected it. Moreover, we present new results on the ionised phase, including the high ionisation coronal gas. All the results are discussed in the context of prior studies of 4C12.50. This work is based on Gran Telescopio Canaria (GTC) K-band and Very Large Telescope (VLT) J, H, K bands long slit spectroscopy of the primary western active nucleus. It is also based on ALMA 12-m array CO(2–1) and 220 GHz continuum observations described in Lamperti et al. (2022, programme 2018.1.00699.S; PI: M. Pereira-Santaella; see also Pereira-Santaella et al. 2021).

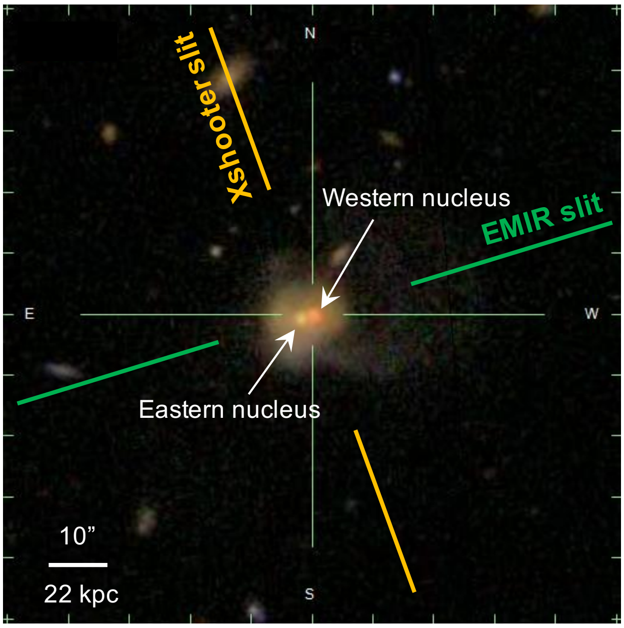

Fig. 1. SDSS colour composite image of 4C12.50 (z = 0.122) with the EMIR (position angle, PA = 104°) and X-shooter (PA = 20°) slit positions overplotted. The double nuclei and the prominent merger features are appreciated clearly. This work is focussed on the western active nucleus.

The paper is organised as follows. We describe the observations and data in Sect. 2. The spectral fitting techniques are explained in Sect. 3. The results of the study of the ionised (including coronal) and the molecular gas components in 4C12.50 are presented in Sect. 4 and discussed in Sect. 5. The summary and conclusions are in Sect. 6.

We adopt H_0 = 69.7 km s^{-1} Mpc^{-1}, Ω = 0.7185 and $\Omega_{\rm m}$ = 0.2877. This gives an arcsec to kiloparsec conversion of 2.20 kpc arcsec^{-1} at z = 0.122.

2. Observations

We obtained K-band spectroscopy of 4C12.50 (RA(2000) 13:47:33.35 and DEC(2000) 12:17:24.2) with the Spanish 10.4 m GTC telescope and the EMIR (Espectrógrafo Multiobjeto Infra-Rojo) instrument in long-slit mode (programme GTC16-21B). EMIR is a near-infrared wide-field imager and medium-resolution multi-object spectrograph installed at the Naysmith-A focal station. It is equipped with a 2048 × 2048 Teledyne HAWAII-2 HgCdTe near-infrared optimised chip with a pixel size of 0.2″. The K grism covers a spectral range of ∼2.03–2.37 µm with a dispersion of 1.71 Å pixel^{-1}.

In order to find a compromise between spectral resolution and flux coverage, the slit width used during the observations was 0.8″, adapted to the K-band seeing size ($FWHM \sim$ 0.8″). The instrumental profile measured from the arc lines is $\rm FWHM_{IP} = 6.32 \pm 0.44$ Å (85.7 ± 6 km s^{-1} at ∼2.2 µm).

The slit position angle, PA 104° N to E, was chosen to align the slit with the two nuclei (Fig. 1). The only line detected from

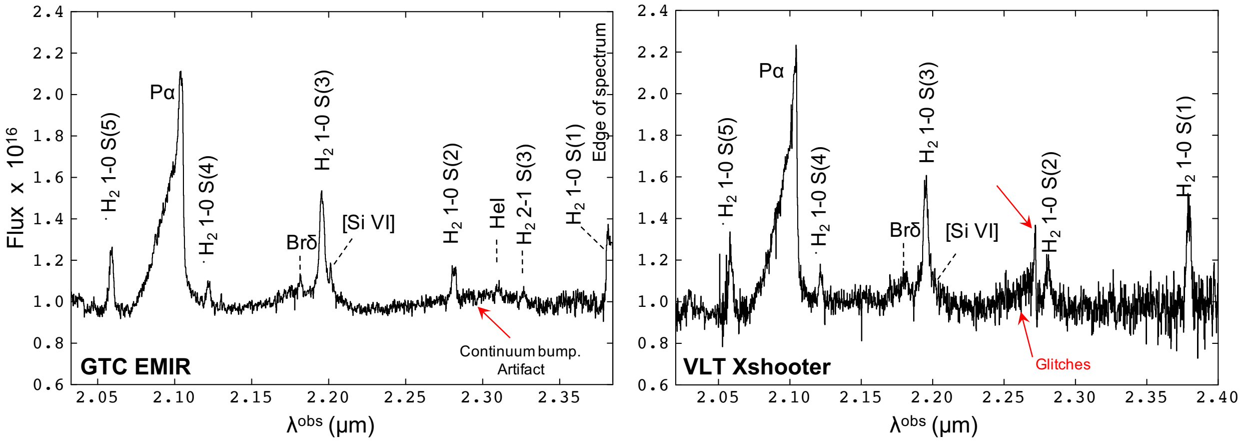

Fig. 2. *K*-band spectrum of 4C12.50. Left: GTC-EMIR (0.8″ × 1.4″ aperture). Right: VLT-X-shooter (1.2″ × 4″ aperture). Flux in units of 10^{-16} erg cm^{-2} s^{-1} Å^{-1}. $\lambda^{\rm obs}$ is the observed wavelength. The red arrows mark artefacts and glitches (see text).

the secondary, eastern nucleus is Paα, which is ∼90 times fainter than that from the primary nucleus. For this reason, we focus our study on the primary nucleus.

Eight spectra were obtained in four different nights (2022 February 12, April 8, 9 and 12). The total exposure time on source was 8×3360 s = 26880 s or 7.5 h. A typical ABBA nodding pattern was applied.

The spectra were reduced using several Python routines customised by GTC staff for EMIR spectroscopic data. The sky background was first subtracted using consecutive A-B pairs. They were subsequently flat-fielded, calibrated in wavelength, and combined to obtain the final spectrum. To correct for telluric absorption, we observed a telluric standard star (HR 5238) with the same observing set-up as the science target, immediately after the 4C12.50 observations and at a similar airmass. To apply the correction, we used a version of Xtellcor (Vacca et al. 2003) specifically modified to account for the atmospheric conditions of Roque de los Muchachos observatory in La Palma (Ramos Almeida & García 2009). Flux calibration was applied using the spectrum of the standard star obtained with a wide 5″ slit.

The *K*-band EMIR spectrum is shown in Fig. 2 (left). A 0.8″ × 1.4″ aperture centred at the continuum centroid of the western nucleus was chosen. This optimises the extraction of the maximum line fluxes and the signal to noise for several important faint lines, so that the kinematic parameters can be constrained more accurately. The strange continuum bump marked with a red arrow in Fig. 2 is an artefact. It suggests a problem with the relative flux calibration in that region of the spectrum. At bluer λ the continuum shape is very similar in the eight spectra and the accuracy of the absolute flux calibration is estimated ∼10%. The shape varies more towards the red. The comparison of the line fluxes in the individual spectra suggests an additional ∼15% uncertainty on the flux calibration in that spectral window (H_2 1–0 S(2) and redder). This will not affect our conclusions. Moreover, we also have the X-shooter NIR spectrum for comparison.

The X-shooter spectrum was described and shown in Rose et al. (2018). It covers the $J + H + K$ spectral range, so that very valuable information can be obtained from additional emission lines (the *K* band range is shown in Fig. 2, right). The spectral resolution values for the 1.2″ slit were 69.2 ± 1.3, 70.1 ± 0.9 and 72.3 ± 1.3 km s^{-1} for the *J*, *H* and *K* bands respectively. The slit was placed at PA 20°, the paralactic angle during the observations (Fig. 1). The pixel scale for the NIR arm is 0.2″. The spectrum was extracted from a 1.2″×4.0″ aperture. This was centred at the western nucleus continuum centroid. The seeing was in the range 0.88″–0.95″ (*g* band). The authors reported a $\lesssim$8% relative flux calibration accuracy.

The X-shooter data have the advantage of covering a much wider spectral range, including very valuable molecular lines in the *J* band, as well as 1–0 S(1). This line lies on the edge of the EMIR spectrum. The advantage of the EMIR spectrum is its higher S/N. The rms values in different continuum windows are in the range $\sim(1.3\text{–}2.6) \times 10^{-18}$ erg s^{-1} cm^{-2} Å^{-1}, ∼1.7–3.5 times lower than for the X-shooter data in the same regions. This spectrum is also more severely affected in some spectral windows by artefacts, including a glitch in the 2.272–2.283 µm range (see Rose et al. 2018 for a detailed explanation). Both spectra are therefore valuable. Galactic extinction is very low ($A_{\rm K} = 0.01$) and no correction was applied for this effect.

In spite of the different aperture sizes, we measure almost identical Paα fluxes in the EMIR ($F_{\rm Pa\alpha} = (1.6 \pm 0.2) \times 10^{-14}$ erg s^{-1} cm^{-2}) and the X-shooter spectra $(1.5 \pm 0.1) \times 10^{-14}$ erg s^{-1} cm^{-2}). The same can be said about most (if not all) *K*-band emission lines (see next section). This suggests that the Paα and other line emission is very compact and strongly concentrated in the primary nucleus and there is little contamination by more extended gas in both apertures.

3. Analysis

Relevant H and H_2 lines detected in the NIR spectrum of 4C12.50 are listed in Tables 1 and 2. Except for Paα and the blend of Brδ, H_2(1–0) S(3) and [SiVI]λ1.9630 (see below), each line flux was measured by integrating the area underneath its spectral profile and above the continuum level. The FWHM were obtained from single Gaussian fits. The SPLOT task in IRAF was used. A single Gaussian provides acceptable fits in general, even when slight asymmetries are hinted.

For complex line profiles and blends (see below), we applied multiple-Gaussian fits using the STARLINK package DIPSO. We used the minimum number of components required to produce an adequate fit, without leaving significant features in the residuals. DIPSO is based on the optimisation of fit coefficients, in the sense of minimising the sum of the squares of the deviations of the fit from the spectrum data. The output from a complete fit consists of the optimised parameters (FWHM, central λ, peak

Table 1. Measurements of H^+ lines in the EMIR and X-shooter spectra of 4C12.50.

Line	λ (µm)	EMIR Flux $\times 10^{-16}$ (ergs cm^{-2} s^{-1})	EMIR *FWHM* (km s^{-1})	EMIR ΔV (km s^{-1})	X-shooter Flux $\times 10^{-16}$ (ergs cm^{-2} s^{-1})	X-shooter *FWHM* (km s^{-1})	X-shooter ΔV (km s^{-1})
Paα(vn)	1.8756				4.3±0.6	101±12	+167±9
(n)	1.8756	29.5±1.1	438±9	0	22.8±2.9	419±18	0
(i)		29.4±2.4	1023±45	−532±24	28.9±2.8	1029±62	−528±35
(b)		98.2±3.5	2707±51	−1441±43	99.0±4.5	2783±53	−1371±46
Paβ	1.2822	Out	Out	Out	52.7±4.7	ns	ns
Brγ	2.1661	Out	Out	Out	12.5±2.5	ns	ns

Notes. For Paα (vn), (n), (i) and (b) refer to the 'very narrow' (only confirmed in the X-shooter spectrum), 'narrow', 'intermediate' and 'broad' kinematic components isolated in the spectral fits. ΔV is the velocity shift of the individual kinematic components of Paα relative to the narrow one (n), which is at the systemic $z_{\rm sys}$. 'ns' means noisy and 'out' means that the line is outside the spectral range.

Table 2. Measurements of the H_2 emission lines detected in the EMIR and-or X-shooter spectra of 4C12.50.

Line	λ (µm)	EMIR Flux $\times 10^{-16}$ (ergs cm^{-2} s^{-1})	EMIR *FWHM* (km s^{-1})	X-shooter Flux $\times 10^{-16}$ (ergs cm^{-2} s^{-1})	X-shooter *FWHM* (km s^{-1})
H_2 2–0 S(1)	1.1622	out	out	2.20±0.21	455±35
H_2 1–0 S(7)	1.7480	out	out	5.10±0.37	461±23
H_2 1–0 S(5)	1.8358	11.4±0.40	471±8	12.50±0.60	465±15
H_2 1–0 S(4)	1.8920	3.65±0.18	424±17	4.31±0.15	389±14
H_2 1–0 S(3)	1.9576	20.1±0.3	418±12	16.7±0.4	424±21
H_2 1–0 S(2)	2.0338	6.03±0.24	453±9	5.51±0.84	457±66 (ns)
H_2 1–0 S(1)	2.1218	20.0±1.9	446±26	21.30±1.10	435±9

Notes. H_2 1-0S(1) is on the red edge of the EMIR spectrum. The S(3) measurements are based on a simple, 1-Gaussian fit of the line profile above the broad pedestal.

and integrated fluxes) and their errors. These were calculated in the linear approximation, from the error matrix. All FWHM values were corrected for instrumental broadening by subtracting the instrumental profile in quadrature.

3.1. The Paα line

The Paα line shows a very prominent blue broad wing (Fig. 3). Three kinematic components are identified in the multi-Gaussian fit of the EMIR spectrum. Their FWHM and velocity shifts relative to the narrow component are shown in Table 1. The results obtained with the X-shooter spectrum are in good agreement (Table 1). The only difference is that an additional, very narrow component ($FWHM$ = 101 ± 12 km s^{-1} and redshifted by +167 ± 9 km s^{-1}) is isolated in these data set. It can be due to the higher spectral resolution, or the different position angle and width of the X-shooter slit. This spectrum may pick up an additional narrow component. It only contributes ~2% of the total line flux.

Holt et al. (2003, see also Holt et al. 2011; Rodríguez Zaurín et al. 2013; Rose et al. 2018) found relatively similar complex kinematics for the strongest optical emission lines from the western nucleus, including forbidden transitions such as [NeV]λ3426, [OIII]$\lambda\lambda$4959,5007, [OI]λ6300 and [SII]$\lambda\lambda$6716,6731 ([NeV], [OIII], [OI] and [SII] hereafter). The three components isolated in the [OIII] doublet have $FWHM$ = 340 ± 23 (narrow), 1255 ± 12 (intermediate) and 1944 ± 65 km s^{-1} (broad), with these last two shifted by −402 ± 9 and −1980 ± 36 km s^{-1} relative to the narrow, systemic component. Rose et al. (2018) identified an additional, even more extreme component in the [OIII] lines using the X-shooter spectrum mentioned here. It has $FWHM$ = 3100 ± 200 km s^{-1} and ΔV = −331 ± 60 km s^{-1}. This fourth component is not apparent in the Paα fit of either the EMIR or the X-shooter spectra and thus we do not consider this option further.

The Paα narrow component has z = 0.12175 ± 0.00008. This is consistent with the z of the narrow [OIII]λ5007 ($z_{\rm sys}$ = 0.12174 ± 0.00002). According to Holt et al. (2003), this component is at the systemic z implied by the stars. It is also consistent within the errors with the CO(2–1) redshift z = 0.121680 ± 0.00004 (Lamperti et al. 2022). In what follows, we also assume that the narrow Paα component is at $z_{\rm sys}$.

3.2. The Brδ+H_2 S(3)+[SiVI] blend

A broad pedestal is apparent underneath Brδ (1.9451 µm), H_2 (1–0) S(3) and [SiVI]λ1.9630 (Fig. 4). Our aim is to discern its nature, since it reveals very high-velocity gas that may trace a coronal and-or molecular outflow. It is also necessary to constrain the flux of the S(3) line.

Due to the complex blend of lines, it is not possible to apply a multiple Gaussian fit avoiding degeneracies. We have applied a different method consisting of creating an artificial Brδ that we subtracted from the original data, as explained below. We then fitted the residual spectrum, which should retain the contribution of S(3) and [SiVI]. This method was applied to both the EMIR and the X-shooter spectra.

To create the expected artificial Brδ profile for a given spectrum, we assumed the same spectral shape as Paα. The differential reddening of the three kinematic components

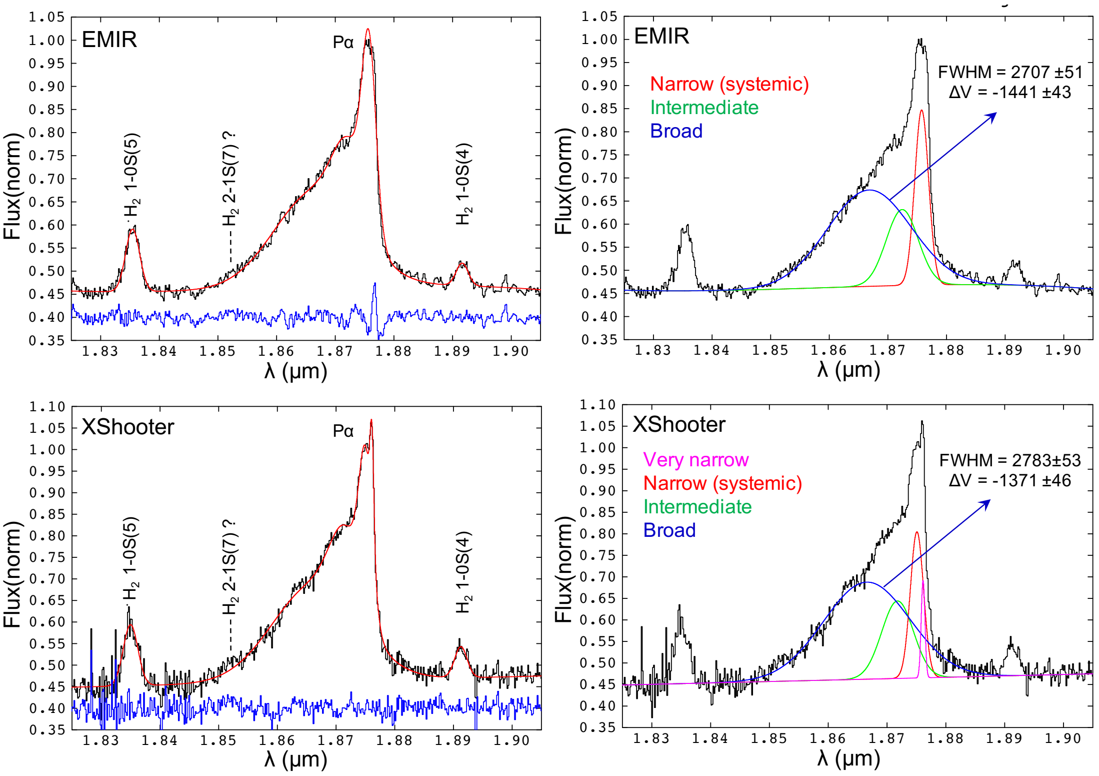

Fig. 3. Fit of Paα using the 0.8″ × 1.4″ EMIR (top) and 1.2″ × 4.0″ X-shooter (bottom) rest frame spectra. Left panels: data (black), fit (red) and residuals (blue), shifted on the vertical axis for visualisation. The small excess of flux on the blue wing of Paα may be H_2 2-1S(7) λ1.8523. Right: Individual components of the fit of Paα, where the values of FWHM and ΔV in km s^{-1} (velocity shift relative to the narrow or systemic component, in red) refer to the broadest (blue) kinematic component. It is due to a prominent ionised outflow. The spectra in these and all other figures have been normalised by the peak flux of Paα.

(Holt et al. 2003, 2011) does not affect the line profile significantly. For E_{B-V} = 0.59 ± 0.11 (as derived by Hα/Hβ, Paα/Hβ and Paβ/Hβ, Rose et al. 2018), the expected flux ratio Paα/Brδ ∼ 18.1 is very close to the case B value, 18.29 (Osterbrock & Ferland 2006). Thus, we used the fitted Paα profile (see previous section), shifted it to the Brδ wavelength and divided its flux by 18.1. The expected Brδ contribution is shown in Fig. 4, together with the continuum fitted by interpolating between the blue and red sides of the line blend. The results of subtracting Brδ from the original spectra are. A broad pedestal is still obvious in both cases.

We then fitted this new spectrum with the smallest number of components (three) that provides a reasonable fit to the residual blend. The results are shown in Table 3 and Fig. 5. The two narrower components correspond to H_2 S(3) and the core of [SiVI].

The pedestal is consistent with a very broad component with $FWHM$ = 3500 ± 375 km s^{-1} for the EMIR spectrum (values for X-shooter will be given in brackets: 3355 ± 247 km s^{-1}). One possibility is that it is dominated by a molecular outflow, blueshifted by −425 ± 83 (−478 ± 136) km s^{-1} relative to the narrow S(3) component. The fact that it is not detected in other molecular lines is not in contradiction. If its contribution relative to the narrow component was similar in all H_2 lines ($F_{\rm broad}/F_{\rm narrow}$ ∼ 1.15 (1.07), as in S(3)), the expected fluxes would be below, or just close to the 3σ detection limits in all cases.

While we cannot unambiguously rule out a broad H_2 S(3) component, the very turbulent kinematics of the ionised gas (Paα, [OIII], etc.) suggests that the broad pedestal is dominated by a coronal [SiVI] outflow. An intermediate situation, with contribution from both broad S(3) and [SiVI], or even contamination by [Si XI]λ1.9359 on the blue side of the blend, could also be possible. Overall, this just reflects the difficulty to deblend the Brδ +H_2 S(3)+[SiVI] lines.

In spite of this, several arguments support the idea that the pedestal is due to a coronal outflow. In this case, the line would consist of two components, both blueshifted relative to $z_{\rm sys}$ (Table 3). The blueshift of both components may indicate that the whole [SiVI] emitting gas (and not only the broad component) is outflowing, although asymmetries in the spatial and-or velocity distributions of the systemic coronal gas cannot be discarded. The broad component (the pedestal) has a blueshift of $\Delta V_{\rm sys}$ = −1296 ± 133 km s^{-1} (EMIR) or −1398 ± 136 km s^{-1} (X-shooter) and it contributes 83 ± 11% of the total [SiVI] flux. This interpretation is supported by the similar kinematics of the coronal [FeVII]λ6087 line (Fig. 6, Table 3). The profile is very broad, asymmetric, and clearly blueshifted relative to $z_{\rm sys}$. Two components are isolated, both broad and blueshifted. The broadest has $FWHM$ = 3071 ± 185 km s^{-1} and ΔV = −912 ± 201 km s^{-1}. It contributes 85 ± 9% of the total line flux. Thus, [FeVII]λ6087, as [SiVI], appears to be dominated by outflowing gas of rather extreme kinematics. Finally, Spoon et al. (2009) found also very turbulent kinematics for the MIR coronal [NeV]λ14.32 μm ($FWHM$ = 2300 ± 190 and ΔV = −1120 ± 89 km s^{-1}). Higher S/N and higher spectral resolution would probably reveal a kinematic substructure consistent with [FeVII] and [SiVI].

In this scenario, the ratio of the total line fluxes is Paα/[SiVI]∼5.4. Similar values have been observed in other type 2 quasars (QSO2) and Seyfert 2 (e.g. Riffel et al. 2006;

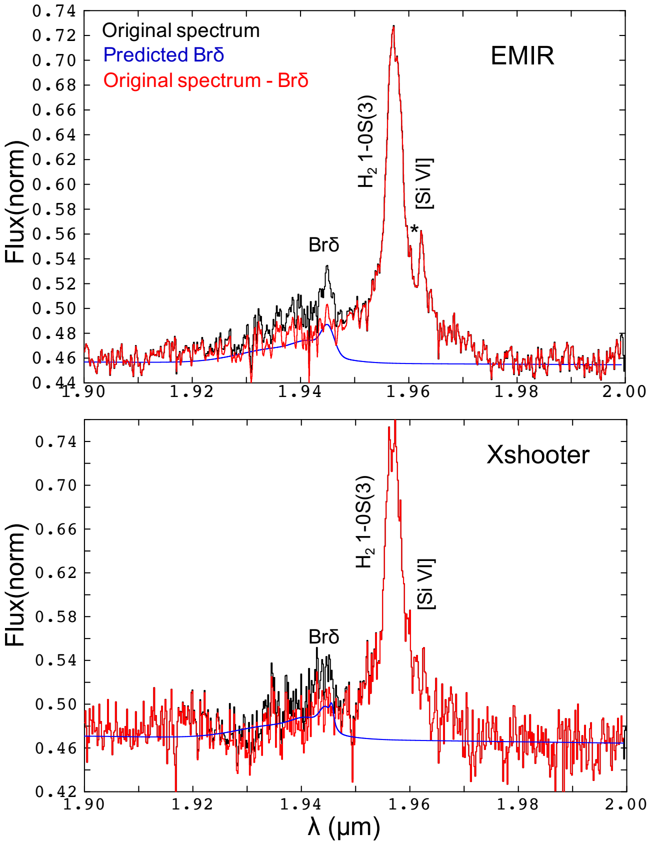

Fig. 4. Brδ, H_2 (1–0) S(3) and [SiVI] blend (black) in the EMIR (top) and X-shooter (bottom) rest frame spectra. The blue line shows the predicted Brδ profile (+ continuum; see text). The results of subtracting Brδ from the original spectra are shown in red. The * marks the location of (or near) a possible artefact in the EMIR spectrum, responsible for the unexpectedly narrow [SiVI] peak.

Ramos Almeida & García 2009; Ramos Almeida et al. 2019). This ratio would be anomalously high (~31) if the pedestal had no [SiVI] contribution. The luminosity of [SiVI], $L_{\rm [SiVI]}$ = $(1.15 \pm 0.07) \times 10^{41}$ erg s^{-1}, is amongst the highest measured in active galaxies (Rodríguez-Ardila et al. 2011; Lamperti et al. 2017; Riffel et al. 2006; Cerqueira-Campos et al. 2021; den Brok et al. 2022). This is not surprising, since most published [SiVI] measurements correspond to less luminous AGN (Seyfert galaxies), while 4C12.50 is a QSO2 (Sect. 1). SDSS J0945+1737, another QSO2 at z = 0.128, has a similarly high $L_{\rm [SiVI]} \sim 1.3 \times 10^{41}$ erg s^{-1} (Speranza et al. 2022). Lamperti et al. (2017) found a weak correlation between the [OIII] and [SiVI] fluxes (in log) for a sample of nearby ($z < 0.075$) AGN (see Fig. 8 in that paper). 4C12.50 is well within the scatter of this relation. We therefore propose that the H_2 S(3) emission is traced by the narrow S(3) above the pedestal, while this feature (possibly the whole [SiVI] flux) is dominated by a coronal outflow.

4. Results

4.1. The warm ionised and coronal gas

The extreme Paα kinematics are roughly consistent with those seen in the optical lines, including the forbidden ones (Sect. 3.1). This implies that the broad Paα (FWHM ~ 2750 km s^{-1} and $\Delta V = -1400 \pm 43$ km s^{-1} (see Table 2) is not emitted by the broad line region (see also Rupke et al. 2005). It is instead emitted by the kinematically extreme ionised compact outflow, whose radial size ~69 pc was measured by Tadhunter et al. (2018) based on HST narrow band emission line images. The broadest component contributes 63 ± 3% of the total Paα flux. Considering the intermediate component also as part of the outflow, as those authors, this value raises to 81 ± 4%.

Holt et al. (2011) inferred a very high density n for the broad component. Using the transauroral emission lines [S II]$\lambda\lambda$4068,4076 and [O II]$\lambda\lambda\lambda\lambda$7318,7319,7330,7331 they obtain $n = (3.16^{+1.66}_{-1.01}) \times 10^5$ cm^{-3}, compared with $n = (2.94^{+0.71}_{-1.03}) \times 10^3$, $(1.47^{+0.60}_{-0.47}) \times 10^4$ cm^{-3} for the narrow and the intermediate components respectively (see also Rose et al. 2018). With these values, and using the reddening-corrected Paα luminosities, we calculate the mass of each kinematic component as:

$$M = \frac{L_{\rm H\beta}\, m_{\rm p}}{\alpha^{\rm eff}_{\rm H\beta}\, h\, \nu_{\rm H\beta}\, n}, \tag{1}$$

where $L_{\rm H\beta}$ is the Hβ luminosity, inferred from the reddening corrected $L_{\rm Pa\alpha}$ and assuming case B $\frac{\rm Pa\alpha}{\rm H\beta}$ = 0.332 (Osterbrock & Ferland 2006), $m_{\rm p}$ is the mass of the proton, $\alpha^{\rm eff}_{\rm H\beta} = 3.03 \times 10^{-14}$ cm^{-3} s^{-1} is effective Case B recombination coefficient of Hβ for T = 10 000 K and $n = 10^4$ cm^{-3} (Osterbrock & Ferland 2006), h is Planck's constant, $\nu_{\rm H\beta}$ is the frequency of Hβ, and n is the electron density. The total mass is $M_{\rm HII} \sim 9.0 \times 10^5\ M_\odot$, of which ~6% corresponds to the broadest component and ~28% to the total outflowing gas (broad+intermediate components).

We plot in Fig. 7 the observed relative contribution of the broadest component to the total line fluxes $\frac{F_{\rm br}}{F_{\rm tot}}$ against the critical density $n_{\rm crit}$ for all the forbidden lines with this information available. Although with a large scatter, a correlation is clear[1]. The emission from the most turbulent gas is much stronger (dominant) in lines with high $n_{\rm crit}$ such as the coronal lines than in low $n_{\rm crit}$ lines, specially those with $n_{\rm crit}$ lower than the outflow density (e.g. [OII]λ3727 with $n_{\rm crit}$=1300 and 4500 cm^{-3} for the two doublet components and [SII]$\lambda\lambda$6716,6731, $n_{\rm crit}$=1500 and 4000 cm^{-3}). This is consistent with the frequent finding that AGN outflows have a more prominent signature in coronal features compared with other lines from both the ionised and specially the molecular phases (De Robertis & Osterbrock 1984; Rodríguez-Ardila et al. 2002; Álvarez-Márquez et al. 2023).

A similar correlation was found in MRK477, the nearest QSO2 at z = 0.035 by Villar Martín et al. (2015). The NLR density is expected to decrease with distance from the AGN (e.g. Bennert et al. 2006; see also De Robertis & Osterbrock 1984). The authors proposed that the outflow in MRK477 has been triggered at ≲220 pc, possibly at ≲30 pc, from the AGN (also by the radio jet) and the correlation shows how its emission weakens as it propagates outwards from the inner denser coronal region (e.g. Müller Sánchez et al. 2006; Rose et al. 2011) outwards in the NLR, following the decreasing density gradient. We propose a similar scenario for 4C12.50.

This also suggests that a single mechanism (the radio jet in this case) is responsible for the outflow identified in all emission lines emitted by the ionised phase, from the coronal to the lowest ionisation species. This is also supported by the similar, unusually high values of $V_{\rm max} = |\Delta V_{\rm sys} - FWHM/2|$ (a frequent definition of the maximum outflow velocity, computed for the

---

[1] The correlation is weaker with ionisation potential. It is not shown for simplicity.

Table 3. Fit of the H_2 (1–0) S(3)+[SiVI] blend using the EMIR spectrum, after removal of the Brδ contribution (Fig. 3, right) and assuming the pedestal is dominated by [SiVI] emission.

Line	λ (μm)	Flux ($\times10^{-16}$ erg s^{-1} cm^{-2})	*FWHM* (km s^{-1})	ΔV (km s^{-1})
EMIR				
H_2 S(3)	1.8756	21.1±0.3	487±35	−42±9
[SiVI]	1.9630	5.07±0.88	510±122	−120±44
Pedestal	1.9630	24.2±2.2	3500±375	−1296±133
X-shooter				
H_2 S(3)	1.8756	19.8±1.8	498±43	−90±21
[SiVI]	1.9630	3.96±1.64	637±203	−313±133
Pedestal	1.9630	21.2±1.8	3355±247	−1398±136
[FeVII] (n)	0.6087	1.28±0.28	828±121	−366±143
(br)	0.6087	7.06±0.51	3071±185	−912±201

Notes. The results of the [FeVII] spectral fit are also shown for comparison. ΔV is computed for this line relative to the narrow component of Hα as measured in the optical X-shooter spectrum where [FeVII] is detected.

most blueshifted component; Rupke et al. 2005) for most lines (Table 4).

The narrow Paα component is at the systemic redshift (Sect. 3.1). The prominent blue excess and the almost total lack of redshifted emission (Fig. 3) could be due to an asymmetric spatial distribution of the outflowing gas. This is expected in 4C12.50, since the interaction between the radio source and the ambient gas at both sides of the AGN is indeed very asymmetric (Morganti et al. 2004).

Another possibility is that the receding side of the outflow is almost completely extinguished by dust. Let us consider the broadest, most turbulent component. If the gas moving away on the far side of the nucleus has the same kinematics and emits the same intrinsic Paα flux as the approaching side (~2.1×10^{-14} erg s^{-1} cm^{-2}, corrected for reddening with $E_{\rm B-V}$ = 1.44 mag, Holt et al. 2003), the comparison with the 3σ upper limit $\lesssim$9.4 × 10^{-16} erg s^{-1} cm^{-2}, implies $E_{\rm B-V}$ >5.8 or $A_{\rm V}$ > 23.5 mag. Assuming the same gas-to-extinction ratio as in our Galaxy (Zhu et al. 2017), this corresponds to a column density of HI, $N_{\rm HI} \sim 2.08 \times 10^{21} \times A_{\rm V}$ cm^{-2} $\gtrsim 4.9 \times 10^{22}$ cm^{-3}, which is consistent with $N_{\rm HI}$ measurements in the central region (~200 pc) of 4C12.50 (Morganti et al. 2013).

Therefore, it is possible that the receding ionised outflow is completely extinguished. This would not be surprising, given the dusty circumnuclear environment of this and other ULIRGs and the presence of a circumnuclear torus related to the AGN. The outflow, therefore, could be truly kinematically extreme in this case, with $FWHM \sim 2 \times FWHM_{\rm broad} \sim 5400$ km s^{-1} (~7000 km s^{-1} for the coronal gas, Table 3), only comparable to those seen in a handful of high z extremely luminous quasars (Perrotta et al. 2019; Villar Martín et al. 2020). The outflow mass, $M \sim 2.5\times10^5$ $M_\odot$ (broad and intermediate Paα components, see above), the mass outflow rate, $\dot{M}$ and the kinetic power $\dot{E}_{\rm kin}$ would still be moderate. These are calculated as (e.g. Rose et al. 2018):

$$\dot{M} = \frac{M\,V}{r} \tag{2}$$

and

$$\dot{E} = \frac{\dot{M}}{2}V^2, \tag{3}$$

where V is the average velocity of the outflowing gas and r is the outflow radius. We assume $V = V_{\rm max}$ (Rupke et al. 2005). For a Gaussian of a given FWHM centred at $V_{\rm sys}$, $V_{\rm max} = FWHM/2$. In the current scenario, $V_{\rm max} \sim 2783$ km s^{-1} and ~1029 km s^{-1} for the broadest and intermediate components respectively (Table 1). Assuming r = 69 pc (Tadhunter et al. 2018), then $\dot{M} \sim 3.3$ $M_\odot$ yr^{-1} and $\dot{E} \sim 1.1 \times 10^{43}$ erg s^{-1} for the broad component; $\dot{M} \sim 4.4$ $M_\odot$ yr^{-1} and $\dot{E} \sim 2.0 \times 10^{42}$ erg s^{-1} for the intermediate component. In total, $\dot{M} \sim 7.7$ $M_\odot$ yr^{-1} ($\ll$SFR ~ 100 $M_\odot$ yr^{-1}, Rupke et al. 2005) and $\dot{E} \sim 1.3 \times 10^{43}$ erg s^{-1}, which is ~0.14% of the bolometric luminosity $L_{\rm bol} \sim 9 \times 10^{45}$ ergs. The values are still moderate (see also Holt et al. 2011; Rose et al. 2018). Given, in addition, the small size (much smaller than the effective radius of the western bulge component, 2.59 ± 0.58 kpc, Dasyra et al. 2006) and volume apparently affected by the ionised outflow, it is not clear whether it will affect the evolution of the host galaxy.

4.2. The hot molecular gas

4.2.1. Rotational temperature, $T_{\rm rot}$

We have calculated the H_2 rotational excitation temperature, $T_{\rm rot}$, using the extinction corrected fluxes and upper limits of the NIR H_2 lines and following Pereira-Santaella et al. (2014). The molecular lines are not necessarily affected by the same extinction as the ionised gas emission. To estimate $E^{\rm mol}_{B-V}$, we have used $\frac{H_2\ 2\text{–}0\ S(3)\lambda1.1175}{H_2\ 2\text{–}1\ S(3)\lambda2.0735}$, which has a theoretical value of 0.83. Both lines are detected in the X-shooter spectrum. Because they are faint and noisy, different aperture sizes were attempted to maximise the S/N. We infer a value of 0.58 ± 0.05. This implies $E^{\rm mol}_{B-V}$ = 0.35 ± 0.08, which is not significantly different in comparison with the ionised gas total extinction $E(B - V)$ = 0.59 ± 0.11 (Holt et al. 2003; Rose et al. 2018).

We show in Fig. 8 the result of modelling the relative population levels of the NIR H_2 lines using single excitation-temperature LTE models (see Pereira-Santaella et al. 2014). We infer $T_{\rm rot}$ = 3020 ± 160 K. This is quite high in comparison with typical values in nearby AGN and ULIRGs. As an example, Riffel et al. (2021) obtained $T_{\rm rot}$ in the range ~760–2075 K in a sample of 36 nearby Sy1 and Sy2 ($0.001 \lesssim z \lesssim 0.056$) selected among the hard X-ray (14–195 keV) sources in the *Swift* Burst Alert Telescope (BAT) survey (Oh et al. 2018). The ULIRGs analysed by Davies et al. (2003), which also host very large $M_{\rm hot}$ (see next section), have maximum temperatures of

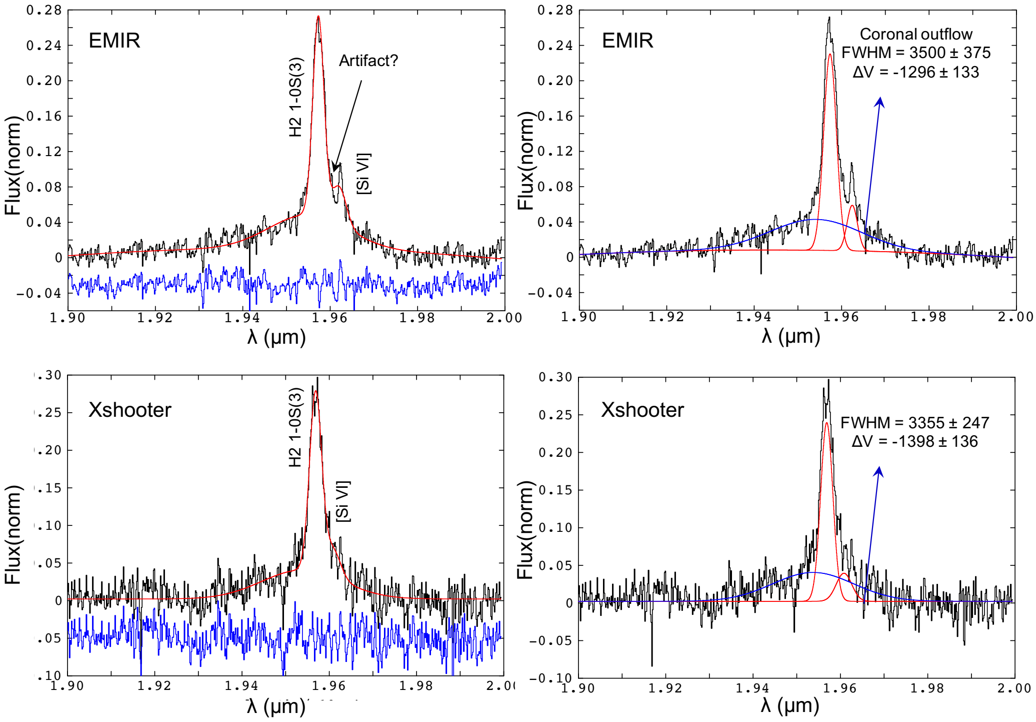

Fig. 5. Fit of the H_2 (1–0) S(3) and [SiVI] blend based on the EMIR (top) and the X-shooter (bottom) spectra, after subtracting the continuum and the contribution of Brδ. The data, fit and residuals are shown on the left panels. The individual components of the fit are shown on the right panels. Colour code as in Fig. 3. The FWHM and ΔV relative to z_{sys} correspond to the broadest component (blue), which is responsible for the broad pedestal.

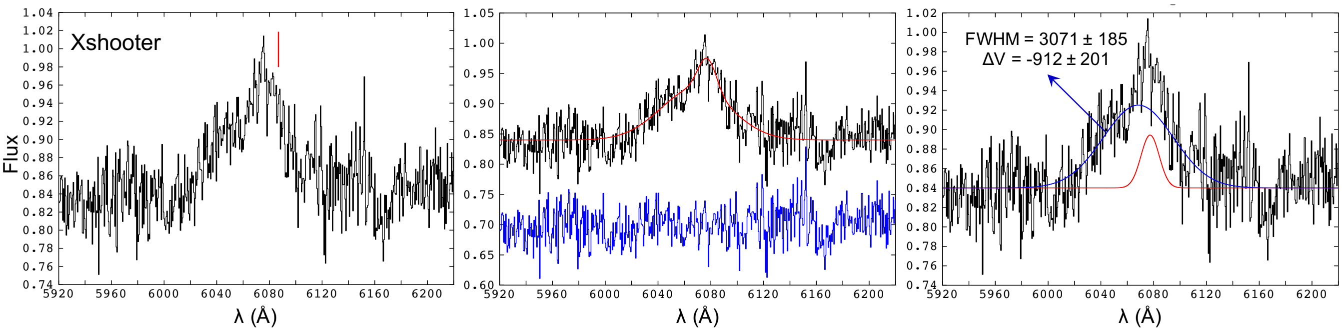

Fig. 6. X-shooter rest-frame optical spectrum centred on [FeVII]λ6087. Left: data. The red vertical line marks the expected location of the line for z_{sys}. The line is clearly blueshifted. Middle: data with fit (red) and residuals (blue, shifted vertically for visualisation). Right: data with the two kinematic components isolated in the fits. The FWHM and ΔV relative to z_{sys} correspond to the broad most blueshited component. Flux in arbitrary units.

~2400 K. In general, $T_{rot} < 2500$ K in galaxies, including U/LIRGs and AGN, (Murphy et al. 2001; Davies et al. 2003; Rodríguez-Ardila et al. 2004, 2005; Ramos Almeida & García 2009; Mazzalay et al. 2013; Pereira-Santaella et al. 2014). Such high temperature is not found either in hot molecular outflows ($T_{rot} \sim 1900$–2300 K), although there is only a handful of objects where it has been possible to isolate the NIR H_2 outflow emission (Emonts et al. 2014; Tadhunter et al. 2014; Ramos Almeida et al. 2019).

The NIR H_2 lines extend the gradient found by Guillard et al. (2012) in 4C2.50 to higher temperatures. They fitted three components using the MIR H_2 lines with $T \sim 100$, 275 and 1500 K respectively. A power-law temperature gradient exists in the molecular gas of numerous galaxies (Davies et al. 2003; Ogle et al. 2010; Guillard et al. 2012; Pereira-Santaella et al. 2014; Togi & Smith 2016).

4.2.2. Mass

The mass of hot molecular gas, $M^{hot}_{H_2}$, can be estimated from the extinction corrected S(1) flux, $F_{H_2 1-0S(1)}$, under the assumptions of local thermal equilibrium and an excitation temperature of 3020 ± 160 K (e.g. Scoville et al. 1982; Riffel et al. 2014). We infer $F_{H_2 1-0S(1)} = (2.44 \pm 0.41) \times 10^{-15}$ erg s^{-1} cm^{-2} (we use the X-shooter line flux in this calculation because it is more accurate), assuming $E_{B-V} = 0.35 \pm 0.08$ (see Sect. 4.2.1). If the gas was not thermalised, the mass would be underestimated.

We obtain $M^{hot}_{H_2} = (2.10 \pm 0.44) \times 10^4\ M_\odot$. We show in Fig. 9 $M^{hot}_{H_2}$ vs. L_{IR} for Riffel et al. (2021) sample of nearby Seyfert 1 and 2 previously mentioned (Sect. 4.2.1). Mass values are also shown for several ULIRGs from Davies et al. (2003) and Piqueras López et al. (2012). $M^{hot}_{H_2}$ of 4C12.50 is at the high end of values found in galaxies, including active

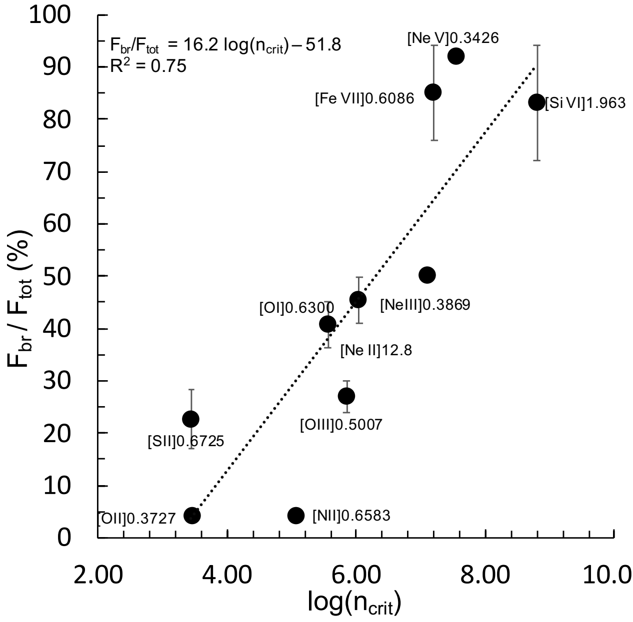

Fig. 7. Relative contribution of the broadest component to the total line fluxes, $\frac{F_{\rm br}}{F_{\rm tot}}$, vs. critical density, $n_{\rm crit}$, in log and cm^{-3}. The dotted line is the linear fit. $\frac{F_{\rm br}}{F_{\rm tot}}$ values are from: this work ([SiVI] and [FeVII]); Holt et al. (2003) and Rodríguez Zaurín et al. (2013, optical lines) and (Guillard et al. 2012, [NeII]12.8 µm). Data with no error bars have no errors available.

Table 4. $V_{\rm max} = |\Delta V_{\rm sys} - FWHM/2|$ (Rupke et al. 2005) of the broadest component for several emission lines.

Line	$V_{\rm max}$ (km s^{-1})	
Paα	2763±53 $^{(a)}$	
[SII]$\lambda\lambda$6716,6731	2803±242 $^{(b)}$	
[NeII]λ12.8	1831±137 $^{(c)}$	
[OIII]λ5007	2952±48 $^{(b)}$	
[OI]λ6300	2431±80 $^{(b)}$	
[FeVII]λ6087	2496±221 $^{(a)}$	
[SiVI]λ1.9623	3076±184 $^{(a)}$	cr

Notes. Values from $^{(a)}$this work, $^{(b)}$Holt et al. (2003), $^{(c)}$Guillard et al. (2012). The lines below Paα are in order of incresing $n_{\rm crit}$.

galaxies and U/LIRGs (see also Rodríguez-Ardila et al. 2005; Piqueras López et al. 2012; Mazzalay et al. 2013; Mezcua et al. 2015; Riffel et al. 2021). It is similar to other nearby ULIRGs and consistent with the value expected from the observed $M^{\rm hot}_{\rm H_2}$ vs. $L_{\rm IR}$ correlation.

If slit losses were significant, the intrinsic mass would be higher, although this situation is unlikely. The hot molecular gas in luminous AGN is usually mostly concentrated within ≲several×100 pc (Mezcua et al. 2015; Riffel et al. 2021). At the z of 4C12.50, such physical size is not resolved spatially in our data. Moreover, since the K-band seeing (see Sect. 2), was significantly narrower than the X-shooter 1.2″ slit, losses are expected to be low in the direction perpendicular to the slit also.

With $\log(L_{\rm IR}/L_\odot) = 12.31$ and $L'_{\rm CO}$ = (1.25 ± 0.38) × 10^{10} K km s^{-1} pc^2 (Dasyra & Combes 2012), 4C12.50 lies close to the $L'_{\rm CO}$ vs. $L_{\rm IR}$ correlation for galaxies and, as other local ULIRGs, it is slightly below it (e.g. Fig. 5 in Cortzen et al. 2019).

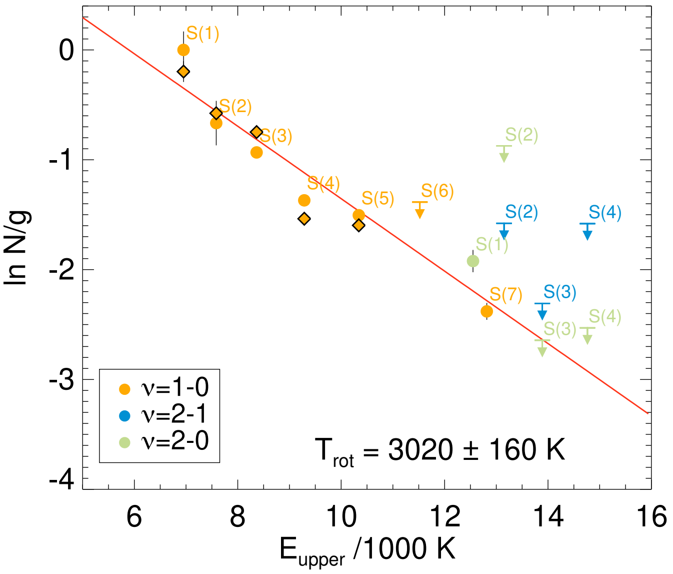

Fig. 8. Modelling the relative population levels of the H_2 NIR transitions using single excitation-temperature LTE models. The orange circles and diamonds represent de X-shooter and EMIR measurements respectively. Upper limits were obtained with the X-shooter spectrum. They correspond to H_2 1–0 S(6) λ1.7880 (orange), the 2–1 transitions (blue) S(2) λ2.1542, S(3) λ2.0729 and S(4) λ2.0041 and the H_2 2–0 transitions (light green) S(2) λ1.1382, S(3) λ1.1175 and S(4) λ1.0998 in the J band. The solid red line shows the single-temperature fit based on the fluxes of the lines detected in the X-shooter spectrum and assuming fully thermalised LTE gas conditions. The EMIR data are shown for comparison.

Thus, $M^{\rm cold}_{\rm H_2}$ = (1.0 ± 0.1) × 10^{10} $M_\odot$ (Dasyra et al. 2014) is also consistent with that expected for its $L_{\rm IR}$ (see Fig. 1 in Daddi et al. 2010a).

The ratio of hot to cold H_2 masses, $\frac{M^{\rm hot}_{\rm H_2}}{M^{\rm cold}_{\rm H_2}}$ = $(2.10 \pm 0.49) \times 10^{-6}$ $M_\odot$, is within the range (~[10^{-7}–10^{-5}]) observed across a sample of several dozen star-forming galaxies and AGN by Dale et al. (2005). It is, moreover, consistent with the value expected from its $\frac{f_{60\,\mu\rm m}}{f_{100\,\mu\rm m}}$ = 0.93 IRAS colour (see Fig. 4 in Dale et al. 2005).

The dependence of $M_{\rm H_2}$ with the excitation temperature, T, is shown in Fig. 10. The mass at $T \sim 3000$ K follows the trend of this and other galaxies, where the bulk of the molecular mass is concentrated at the lowest temperature (Guillard et al. 2012). The mass-temperature function at $T \gtrsim 300$ K is well described in 4C12.50 with a power-law: $M_{\rm H_2}(M_\odot) = 9 \times 10^{17}\ T^{-3.9}$ (coefficient of determination, R^2 = 0.937) or $\frac{{\rm d}M_{\rm H2}}{{\rm d}T} \propto T^{-n}$ with $n \sim 5$. Aperture effects do not have a significant impact in this plot. Although the warm masses (Guillard et al. 2012) were obtained with *Spitzer* IRS data (which provides much larger aperture sizes (3.6″ × 57″ to 11″ × 22″, depending on the line), the gas is expected to be highly concentrated within a spatial region smaller than the physical region covered by the X-shooter aperture (2.6 × 8.8 kpc^2).

A mass-temperature power-law distribution of the molecular gas at $T \gtrsim 100$ K is frequently observed or assumed for galaxies, independently of the excitation mechanism. Togi & Smith (2016) found that a continuous power-law distribution of rotational temperatures, with $\frac{{\rm d}M_{\rm H2}}{{\rm d}T} \propto T^{-n}$, reproduces well the H_2 excitation from a wide range of galaxy types using a single parameter, the power-law slope n (see also

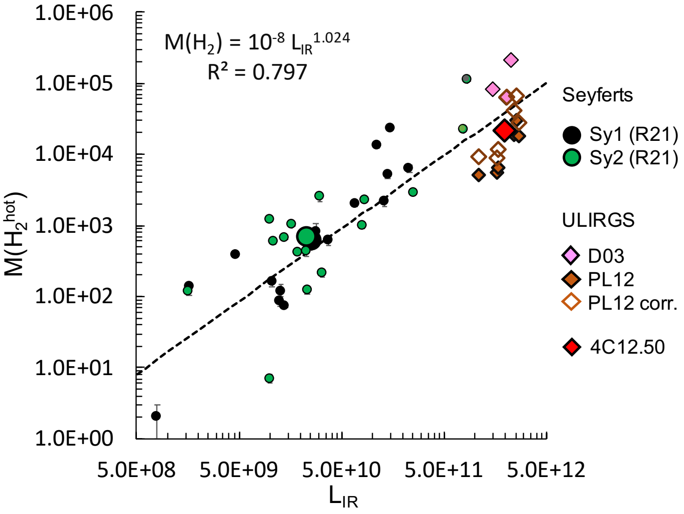

Fig. 9. $M_{\rm H_2}^{\rm hot}$ in units of $M_\odot$ vs. the 8–1000 µm infrared luminosity $L_{\rm IR}$ in units of $L_\odot$. The objects are Sy1 and Sy2 from R21 (Riffel et al. 2021) and ULIRGs from D03 (Davies et al. 2003) and PL12 (Piqueras López et al. 2012). No extinction correction has been applied, except for PL12 ULIRGs (open orange diamonds; PL12 corr.). The same extinction as the ionised gas has been assumed (Piqueras López et al. 2013). 4C12.50 is plotted as a red diamond. The observed and extinction corrected masses are very similar in this case. The size of the symbol is similar to the errorbar. The large black and green solid circles (in an almost identical location) are the median of the Sy1 (small black circles) and Sy2 (small green circles) values. The dotted black line shows the best fit to all solid data points (this is, the masses not corrected for extinction).

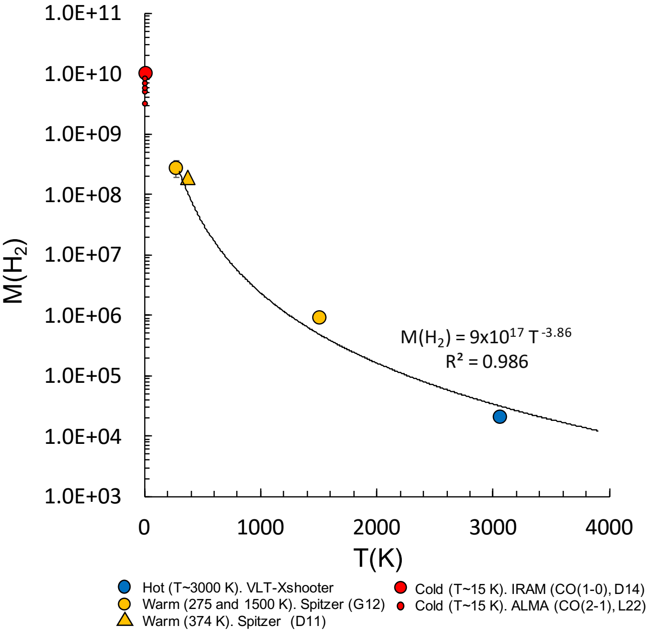

Fig. 10. Dependence of the molecular gas mass in $M_\odot$ with excitation temperature for 4C12.50. The colour code clarifies the tempertature ranges considered as 'cold', 'warm' and 'hot' in this work. The small red circles indicate the cold H_2 masses infered from CO(2–1) ALMA data for different apertures with the radius varying from 0.5″ to 2″ (see text). The black solid line shows the best fit to the warm (G12) and hot data points, with the equation and coefficient of determination, R^2. G12: Guillard et al. (2012); D11: Dasyra & Combes (2011); D14: Dasyra et al. (2014); L22: Lamperti et al. (2022).

Pereira-Santaella et al. 2014). This model, can recover the mass at $T \gtrsim 100$ K, with n in the range 3.79–6.4 and average 4.84 ± 0.61. n gives information on the relative importance of gas heating by shocks, photoelectric heating, UV pumping, etc. According to Neufeld & Yuan (2008) $n \sim 4$–5 is consistent with the predictions of simple models for paraboloidal bow shocks. For 4C12.50, the high $T_{\rm rot}$ and the $n \sim 5$ power-law mass-temperature distribution suggest that shocks play an important role on the excitation of the molecular gas at $T \gtrsim 300$ K.

4.2.3. Excitation mechanism

We have shown that the high $T_{\rm rot}$ and the power-law mass-temperature distribution suggest that shocks play an important role on the excitation of the molecular gas at $T \gtrsim 300$ K. We now check whether the influence of shocks is apparent in the diagnostic diagram [Fe II] $\lambda1.257$ µm/Paβ vs. H_2 1–0 S(1)/Brγ (Larkin et al. 1998; Rodríguez-Ardila et al. 2005; Riffel et al. 2021; see also Colina et al. 2015). [Fe II] $\lambda1.257$ µm/Paβ = 0.73 ± 0.08 for 4C12.50 is obtained from the X-shooter spectrum.

Brγ is outside the observed spectral range of the EMIR data, and very noisy in the X-shooter spectrum. We measure $F_{\rm Br\gamma} = (1.25 \pm 0.25) \times 10^{-15}$ erg s^{-1} cm^{-2} (Table 1) and, thus, S(1)/Brγ = 1.70 ± 0.35. $F_{\rm Br\gamma}$ agrees within the errors with the reddened flux predicted from Paα assuming $E(B-V) = 0.59 \pm 0.11$ (Holt et al. 2003; Rose et al. 2018), $F_{\rm Br\gamma} = (1.43 \pm 0.08) \times 10^{-15}$ erg s^{-1} cm^{-2}. Therefore, S(1)/Brγ = 1.49 ± 0.11.

4C12.50 is in the area of the [Fe II] $\lambda1.257$µm/Paβ vs. H_2 1–0 S(1)/Brγ diagram occupied by AGN. According to Riffel et al. (2021), 0.4≤ H_2 S(1)/Brγ <2 for low excitation AGN; 2≤ S(1)/Brγ < 6 for high excitation AGN and S(1)/Brγ > 6 for shock-dominated regions. Thus, the ratio is typical of high excitation AGN, and it is below values expected for shock-dominated regions.

This, however, does not imply that shocks are not present. A more likely scenario is that a combination of excitation mechanisms exists. 4C12.50 is part of the MOHEG (molecular hydrogen emission galaxy) sample of radio galaxies hosting fast ionised and HI jet-driven outflows studied by Guillard et al. (2012). They discarded AGN X-ray heating as the dominant source of excitation of the MIR H_2 in these systems, based on the large ratio of the H_2 line luminosity (summed over the MIR S(0) to S(3) rotational transitions) to the unabsorbed 2–10 keV nuclear X-ray luminosity (see also Ogle et al. 2010). Instead, shocks are proposed as the main excitation mechanism. Using magnetic shock models, they showed that the dissipation of a small fraction (<10%) of the kinetic energy of the radio jet heats the gas to a range of temperatures (Sect. 4.2.1), and it is enough to power the observed mid-IR H_2 emission.

An important difference between 4C12.50 and most MOHEGs is that it hosts a very luminous AGN (Ogle et al. 2010). Spoon et al. (2009) and Guillard et al. (2012) showed that, while the lower ionisation lines in the MIR are consistent with shocks, the high ionisation lines (in particular [NeV]), arise primarily from photoionisation of the gas by the AGN. The presence of strong coronal lines (Sect. 3.2) indicates that it must contribute to the excitation of at least the ionised gas. This could explain why this system, which is expected to host strong jet-induced shocks affecting the molecular gas (see also previous section), is located in the AGN area of the diagnostic diagram.

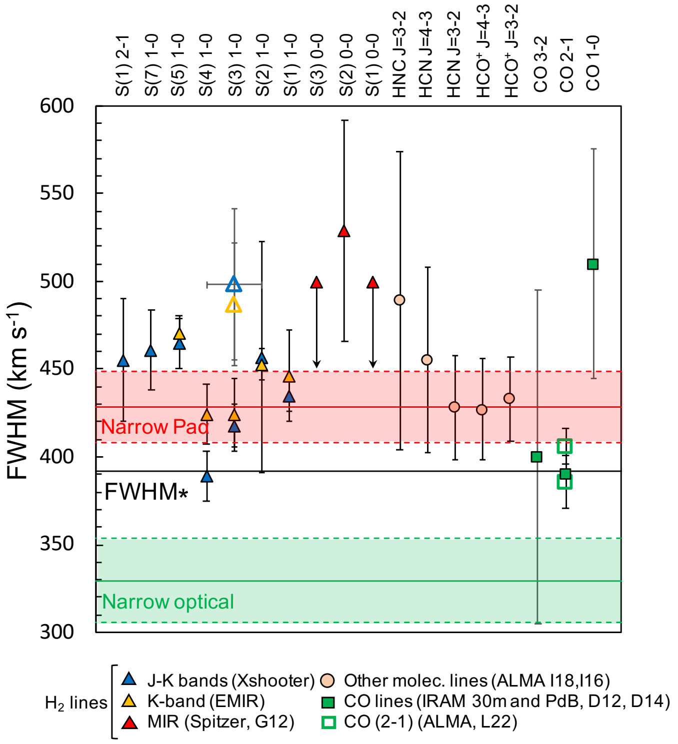

Fig. 11. Intrinsic FWHM of molecular lines detected in 4C12.50. The solid and open triangles for S(3) (1–0) are the values from Tables 2 and 3 respectively. The two green open squares are ALMA CO(2–1) measurements for the nuclear (top, 0.1″ radius aperture) and integrated (bottom, 1.5″ radius aperture) spectra (Lamperti et al. 2022). The solid horizontal black line marks $FWHM_* = 392$ km s^{-1} (Dasyra et al. 2006). The coloured areas correspond to the FWHM (± errors) of the narrow (systemic) component of Paα (red) and the optical (green) ionised gas lines. D12: Dasyra & Combes (2012); D14: Dasyra et al. (2014); G12: Guillard et al. (2012); I16: Imanishi et al. (2016); I18: Imanishi et al. (2018).

4.2.4. Kinematics

Dasyra & Combes (2011) identified prominent blue wings in two out of the three H_2 MIR lines detected in the *Spitzer* spectrum of 4C12.50, H_2(0–0) S(1) at 17.04 µm and S(2) at 12.28 μm. The main component, which they consider to trace the systemic velocity, is spectrally unresolved with $FWHM \lesssim 550$ km s^{-1}. The blue wing is ~2.6 times fainter, it is shifted by $\sim\!-640$ km s^{-1} and has an instrumentally corrected $FWHM \sim 521$ km s^{-1} (errors unavailable). They propose this is produced by an AGN jet or wind-driven outflow. The outflow mass, $5.2 \times 10^7\ M_\odot$, is a high fraction, ~27%, of the total warm (~400 K) H_2 mass. Guillard et al. (2012) also studied the MIR H_2 lines based on *Spitzer* data. They could not confirm the outflow and report the tentative detection of a blue wing in H_2(0–0) S(1) only. We investigate in this section whether the molecular outflow is detected in the NIR H_2 lines.

The hot molecular gas has much simpler kinematics than the ionised gas, whose motions are strongly defined by the outflow triggered by the radio source (Sect. 3.1). The NIR H_2 line profiles are well reproduced by single Gaussians and have instrumentally corrected FWHM with median values $\sim 446 \pm 13$ and 455 ± 10 km s^{-1} for the EMIR and X-shooter spectra respectively (Table 2). No broad components, that may be indicative of an outflow, are detected for any line (see below).

As shown in Fig. 11, the lines emitted by H_2 and other molecular species in 4C12.50 have $FWHM \gtrsim 400$ km s^{-1} (Fig. 11), although some are affected by large uncertainties[2]. The CO(1–0) and H_2 NIR lines are rather broad compared with different types of galaxies at $z < 0.5$, but not extreme if U/LIRGs and active galaxies, including quasars, are considered (Murphy et al. 2001; Rodríguez-Ardila et al. 2004, 2005; Colina et al. 2005; Piqueras López et al. 2012; Riffel et al. 2013; Villar-Martín et al. 2013; Cortzen et al. 2019; Ramos Almeida et al. 2022; Lamperti et al. 2022).

Information on the potential presence of gas turbulence can be obtained by comparing with the stellar FWHM$_*$. As in many interacting systems, complex, non-ordered stellar motions have been identified in 4C12.50 (Perna et al. 2021). Dasyra et al. (2006) measured $FWHM_* = 392 \pm 112$ km s^{-1}, which is affected by a large uncertainty. The narrow (systemic) component of the emission lines from the ionised gas has FWHM=340 ± 23 km s^{-1} for the optical lines (Holt et al. 2003; 319 ± 6 km s^{-1} according to Rose et al. 2018) and $FWHM = 419 \pm 18$ km s^{-1} or 392 ± 15 km s^{-1} for Paα according to the EMIR and the X-shooter spectra respectively (Table 2). All are consistent with FWHM$_*$ within the errors, although the FWHM of the narrow Paα is somewhat broader (3.2σ significance) in comparison with the optical lines. This is not surprising, given the rich dust content of 4C12.50. Slightly larger stellar velocity widths are often inferred for galaxies using NIR stellar features compared with the optical values. This suggests that the NIR features probe more deeply embedded (and therefore higher velocity dispersion) stellar populations than the optical ones (Caglar et al. 2020).

Depending on which value we use (Fig. 11), the molecular lines are all broader than the narrow optical component or similar to the narrow Paα. This is not likely to be affected by aperture effects, given the diversity of aperture sizes for the data, and the consistency of the result for most lines. Based on this comparison, therefore, it is not possible to confirm whether the hot (neither the warm) H_2 gas shows turbulent motions in relation to the systemic motions.

An indication of turbulence of the warm and hot molecular gas is suggested by the fact that all lines appear to be broader than CO(2–1) and, possibly, CO(1–0). The origin is however unknown. Although the dominant kinematic component of the hot molecular gas in ULIRGs and Seyferts is rotation, non rotational components are often also identified (e.g. Bianchin et al. 2021). They could be gas elements out of dynamical equilibrium, such as gas streams related to galaxy interactions, inflows or outflows (Dasyra & Combes 2011; Guillard et al. 2012; Fotopoulou et al. 2019).

Another result of the kinematic analysis is that a counterpart of the prominent MIR H_2 molecular outflow identified by Dasyra & Combes (2011) is not confirmed. We show next that if the NIR H_2 lines had the same relative contribution of the outflow as in the MIR, we should have detected it.

For this, we have created the expected spectral profiles of H_2 S(5), S(2) and S(1) assuming the same kinematic substructure in km s^{-1} as the MIR lines (instrumental broadening has been taken into account). We then compared these with the data. For S(1), we have used the X-shooter spectrum because the line

---

[2] H_2 0–0 S(0) at 28.22 µm is surprisingly broad $FWHM = 906 \pm 91$ km s^{-1} (Guillard et al. 2012). Because this line is in a noisy part of the *Spitzer* spectrum (see their Fig. 2) and given the inconsistency of its FWHM in comparison with all other molecular lines, we have not considered it.

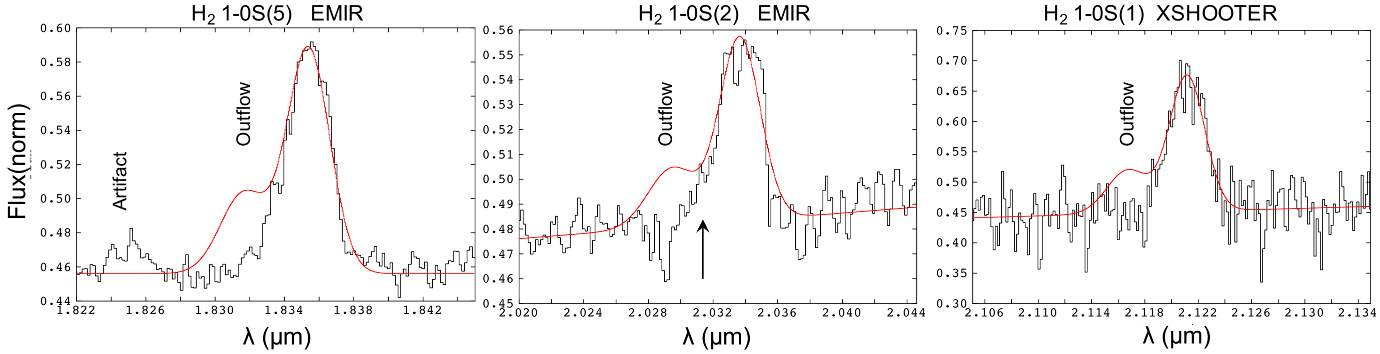

Fig. 12. Observed emission (black) of H_2 S(5) (left), S(2) (middle) and S(1) (right) and the expected profiles (red), for which we assume the presence of a molecular outflow with similar kinematic properties and relative flux contribution as in the MIR H_2 lines. The troughs at the peak of the S(2) and S(1) are due to the noise.

is on the edge of the EMIR data. The results are shown in Fig. 12. The red lines are the expected line profiles. The molecular outflow should have been detected for the three lines as a clear blue excess, but this is not the case.

A faint excess may be hinted on the blue wing of S(2) in the EMIR spectrum (Fig. 12). However, it is not clear this is real, based on the non detection in the X-shooter spectrum, the structure of the noise in adjacent spectral regions, and the absence of the wing in other H_2 lines, both in the X-shooter and EMIR spectra.

In summary, we find no evidence for a hot molecular outflow in the NIR H_2 lines. Kinematic turbulence is suggested by somewhat broader line widths in comparison with CO(2–1) and CO(1–0). The origin of this turbulence can be diverse. Given the clear role of the jet-induced shocks in heating the H_2 gas, it seems natural that they may also affect the kinematics inducing some turbulence (see also Guillard et al. 2012).

It is possible that faint spectroscopic features related to the feedback induced by the jet are lost in the overwhelming glare of the bright nuclear line emission in the spatially integrated spectra analysed in this work. NIR and MIR integral field spectroscopy at very high spatial resolution (for instance with NIRSPEC and-or MIRI on the JWST) would be of key value to map in two spatial dimensions the impact of the interaction between the radio jet and the ambient hot and warm molecular gas with spatial resolution of FWHM ~ several×100 pc.

5. Discussion

Observations of ionised and neutral gas outflows in radio galaxies suggest that AGN radio jet feedback has the potential to affect the gaseous environment of their hosts from nuclear to galactic scales, and out into the circumgalactic medium. This feedback mechanism may also be relevant in systems hosting moderate-power radio sources (e.g. Villar Martín et al. 2017, 2021; Jarvis et al. 2019; Girdhar et al. 2022). To determine whether and how the radio sources can regulate the star formation in their host galaxies, it is necessary to understand how the molecular gas is affected (e.g. Tadhunter et al. 2014; Morganti et al. 2021).

4C12.50 is a very relevant system in this context. If radio-induced feedback can regulate the star formation activity in galaxies, it is a promising candidate to reveal this phenomenon in action. The compact, twin jet is still within the region where a huge accumulation of molecular gas and dust formed during the course of a gas-rich merger, prior to the coalescence with the companion secondary nucleus. This process has favoured intense star formation (see Sect. 1). The large mechanical energy of the powerful radio source and the high concentration of gas have resulted on a strong jet-gas interaction that has triggered kinematically extreme ionised and neutral outflows (Sect. 4.1 and references therein).

The regulation of the system's evolution by the jet may occur, on one hand, by expelling the dusty nuclear cocoon. The system may transition in this way from a ULIRG to an optically less obscured radio galaxy (Sect. 1). On the other hand, the radio source could act on the molecular reservoir by heating (or cooling) gas, which may result in quenching (or triggering) star formation and thus halting (or triggering) the growth of the galaxy.

5.1. Clearing out of the cocoon by the radio jet

Like many local ULIRGs, 4C12.50 hosts an obscured and very compact nucleus. Based on the CO(2–1) ALMA data described in Lamperti et al. (2022), we measure a deconvolved half light radius of the CO(2–1) emission of $r_{\rm CO}$ = 358 ± 2 pc (see also Evans et al. 2002). A molecular gas mass $\log(M_{\rm H2}) = 9.36 \pm 0.05\ M_\odot$ (~23% of the total cold molecular gas mass) is enclosed within. Most of the remaining cold molecular gas is in a ~4 kpc-wide disk (Fotopoulou et al. 2019).

For comparison, compact obscured nuclei with $r_{\rm CO} \sim$ 200−400 pc and $M_{\rm H2}$ ~(0.1-several)×$10^9\ M_\odot$ are common in local ULIRGs (Condon et al. 1991; Soifer et al. 2000; Pereira-Santaella et al. 2021). The small sizes of the twin jet in 4C12.50 (total size ~220 pc) and of the ionised (radial size $r \sim 69$ pc, Tadhunter et al. 2018) and neutral ($r \sim 100$ pc, Morganti et al. 2013) outflows triggered by it, indicate that they are well within the dusty cocoon. Therefore, the clearing up process may be at work.

Currently, the radio plasma appears to be dragging a small fraction of the total cocoon mass, with ~$8 \times 10^5\ M_\odot$ of ionised gas and $1.6 \times 10^4\ M_\odot$ of neutral gas at a total mass outflow rate of ~10 $M_\odot$ yr^{-1} at most (Holt et al. 2011; Morganti et al. 2013; Rose et al. 2018). Considering all studies of the molecular gas component, there is no solid evidence for a molecular outflow in 4C12.50, neither in emission, nor in absorption (Sects. 1 and 4.2.4), not at any temperature, hot (this work), warm or cold. In spite of the clear and dramatic impact of the jet on the ionised and neutral gas kinematics, it has no obvious effects on the kinematics of the hot (neither warm) molecular gas except, possibly, some enhanced turbulence in comparison with the cold molecular gas. This is not enough to remove significant amounts of molecular gas and clear out the central cocoon (Guillard et al. 2012). As discussed by the later authors, this implies that dynamical coupling between the molecular gas and the ionised and neutral outflowing gas is weak.

At the total observed $\dot{M}$, and assuming the unlikely case that all the gas is successfully removed from the central region, the radio source would have to be trapped and removing the gas within the cocoon for an unrealistically long time $\sim 2.3 \times 10^8$ yr. This is as long as the maximum radio source dynamical ages in radio galaxies in general. These are typically $\lesssim$several$\times 10^8$ yr, with the longest ages measured in giant radio galaxies (e.g. Machalski et al. 2007, 2009).

At the moment, it appears that the radio jet is displacing mass at a too slow rate to efficiently clear up the dusty cocoon. It is unclear whether the removal of a significantly lower amount of mass would suffice to promote the transition into an optically less obscured radio galaxy.

5.2. Impact of jet-induced feedback on the star formation activity

It is not clear whether the outflow can affect substantially the star formation activity in 4C12.50, given the moderate mass outflow rate ($\dot{M}$ < SFR), kinetic power and small volume (see Rose et al. 2018 for a detailed discussion). The radio source size is ~220 pc. The affected volume is much smaller than the galactic bulge (the effective radius of the galaxy hosting the western nucleus is $r_{\rm eff} = 2.59 \pm 0.58$ kpc, Dasyra et al. 2006). Star formation may be affected within the inner $r \lesssim 100$ pc, the maximum estimated outflow size, but the impact on larger scales is lacking evidence. As argued by Rose et al. (2018), the presence of a lower density outflow component that has a high mass, and contributes relatively little to the emission line fluxes cannot be ruled out. However, there is currently no observational evidence for it.

Even if a powerful molecular outflow is not triggered, suppression of star formation may occur as a consequence of other processes related to the jet, such as molecular gas heating and-or the injection of turbulence. Evidence for this process lies in the unusually high temperature ($T_{\rm rot} = 3020 \pm 160$ K) of the hot component, the power-law temperature-mass function relation (Sects. 4.2.1 and 4.2.2), and the fact that shocks are needed to explain the MIR H_2 emission (Sect. 4.2.3; Ogle et al. 2010; Guillard et al. 2012). Shocks can be generated in different ways. In ULIRGs in particular, interactions with nearby galaxies can excite large-scale shocks that will cool by means of H_2 emission (Zakamska 2010; Rich et al. 2015). In 4C12.50, a natural scenario is that the compact, powerful jet plays a major role on producing shocks. The clear impact of the interaction with the ionised and neutral components suggests that shocks are indeed present. If the jet encounters molecular gas on its path, it may inject mechanical energy capable of heating it, even if the kinematics is not significantly affected.

We investigate next whether there is evidence for star formation suppression in 4C12.50. Lanz et al. (2016) found that MOHEGs (including 4C12.50) fall below the K–S relation of galaxies, log($\Sigma_{\rm SFR}$) vs. log($\Sigma_{\rm CO}$, Kennicutt 1998). These are the surface density of star formation and the surface density of molecular gas respectively. According to the authors, this suggests that the SFR is suppressed by a factor of 3–6, depending on how the molecular gas mass is estimated. Approximately 25% of their sample shows a suppression by more than a factor of 10. For 4C12.50, they found a factor ~10 in comparison with normal galaxies, and a factor ~100 in comparison with ULIRGs. They suggested that the shocks driven by the radio jets are responsible for the suppression, by injecting turbulence into the interstellar medium (ISM). They also found that the degree of SFR suppression does not correlate with indicators of jet feedback including jet power, diffuse X-ray emission, or intensity of warm molecular H_2 emission.

Using the ALMA data previously mentioned, we have revised the location of 4C12.50 in the K–S relation of different galaxy types. For the purpose of comparison with Lanz et al. (2016), we calculate $\Sigma_{\rm SFR} = \frac{SFR}{\pi r_{\rm SF}^2}$ and $\Sigma_{\rm M_{H_2}} = \frac{M_{\rm H_2}}{\pi r_{\rm H_2}^2}$, where $r_{\rm SF}$ and $r_{\rm H_2}$ are the radial sizes of the star-forming region and of the molecular gas distribution respectively.

The main sources of uncertainty to determine both Σ values come from the uncertain SFR and the areas of the star-forming region and the molecular gas distribution. The main difficulty to estimate the SFR is the uncertain fraction of AGN contribution to $L_{\rm IR}$, $f_{\rm IR} = 100 \times \frac{L_{\rm IR}^{\rm AGN}}{L_{\rm IR}}$. Veilleux et al. (2009) applied six different methods to infer the fraction of AGN contribution to the bolometric luminosity $L_{\rm bol}$, $f_{\rm bol} = 100 \times \frac{L_{\rm bol}^{\rm AGN}}{L_{\rm bol}}$ and obtained values in the range ~28–84%, with an average of 57 %. Perna et al. (2021) constrained the range further to $f_{\rm bol} \sim 60$–82%, depending on the method. Since ~90% of $L_{\rm bol}$ is emitted in the infrared for 4C12.50, we assume $f_{\rm bol} \sim f_{\rm IR}$. The assumption of $f_{\rm IR} \sim 60$–82% is reasonable, also based on the ratio of the mid- to far-infrared continuum fluxes of 4C12.50, $\log(\frac{F_{5-25\,\mu{\rm m}}}{40-122 \mu m}) = -0.19$. This is intermediate between starburst dominated ULIRGs (~–1.25), and AGN dominated ULIRGs (~0.35 Veilleux et al. 2009). This suggests a significant, but not total contamination of a MIR bump due to the AGN (Lanz et al. 2016).

This implies SFR~63–141 $M_\odot$ yr^{-1} (Kennicutt 1998). For comparison Rupke et al. (2005) quote 101 $M_\odot$ yr^{-1}. These SFR values are in the range of other ULIRGs (e.g. Daddi et al. 2010a; De Looze et al. 2014; Perna et al. 2021), and SFR $\gtrsim 100$ $M_\odot$ yr^{-1} is consistent with the value expected for its gas mass (see Fig. 1 in Daddi et al. 2010a). Lanz et al. (2016) fitted the spectral energy distribution (SED) of 4C12.50 with both an AGN and a starburst component, which is essential to obtain a more accurate $f_{\rm IR}$. They inferred SFR ~ 24 $M_\odot$ yr^{-1} for 4C12.50 and, thus, $f_{\rm IR}$ ~93%. This is indeed bellow the value expected for its gas mass. However the authors warn that a combination of dust temperatures not implemented in their method would be more adequate to fit the IR SED. Given all uncertainties, we consider three possibilities: SFR=24, 63 and 141 $M_\odot$ yr^{-1}.

Regarding the areas of the star-forming region and the molecular gas distributions, we have considered several possibilities summarised in Table 5. We measure a half light radius of the CO(2–1) emitting region $r_{\rm CO} = 358 \pm 2$ pc (see previous section). This is very similar to the median value, 320 pc, inferred by Pereira-Santaella et al. (2021) for their sample of nearby ULIRGs. We consider this $r_{\rm CO}$ a reasonable upper limit for $r_{\rm SF}$, since $r_{\rm SF} < r_{\rm CO}$ invariably in ULIRGs (Pereira-Santaella et al. 2021). This is also consistent with MIR observations which indicate that most of the star formation in ULIRGs occurs in very compact regions (<1 kpc; e.g. Soifer et al. 2000; Díaz-Santos et al. 2010; Alonso-Herrero et al. 2016). This implies lower limits for log($\Sigma_{\rm SF}$) of $\gtrsim 1.76$ or $\gtrsim 2.19$ and $\gtrsim 2.54$, depending of the three assumed SFR values for 4C12.50. For comparison, most ULIRGs in Pereira-Santaella et al. (2021) sample are in the range 2.8–4.3[3].

---

[3] For the purpose of this comparison, we have multiplied their values by 2, since they estimate the area as $A = 2\pi r^2$.

Table 5. Surface density of star formation and of cold molecular gas for different assumptions of SFR and radial sizes of the SF ($r_{\rm SF}$) and molecular gas ($r_{\rm H_2}$) distributions.

Case	$r_{\rm H_2}$ (kpc)	$r_{\rm SF}$ (kpc)	$\log(M^{\rm enc}_{\rm H_2})$ ($M_\odot$)	SFR ($M_\odot$ yr^{-1})	$\log(\Sigma_{\rm M_{H_2}})$ ($M_\odot$ pc^{-2})	$\log(\Sigma_{\rm SFR})$ ($M_\odot$ yr^{-1} kpc^{-2})	Symbol
		(A) $r_{\rm H_2} = r_{\rm SF} = r_{\rm CO}$, $\alpha_{\rm CO} = 0.78$					
A1	0.358	0.358	9.36	141	3.76	2.54	Green triangle
A2	0.358	0.358	9.36	63	3.76	2.19	Red triangle
A3	0.358	0.358	9.36	24	3.76	1.76	Black triangle
		(B) $r_{\rm H_2} = r_{\rm SF} = r_{\rm disk}$, $\alpha_{\rm CO} = 0.78$					
B1	2.0	2.0	10.00	141	2.90	1.05	Green circle
B2	2.0	2.0	10.00	63	2.90	0.70	Red circle
B3	2.0	2.0	10.00	24	2.90	0.28	Black circle
		(C) $r_{\rm H_2} = r_{\rm SF} = 4.2$ kpc, $\alpha_{\rm CO} = 4.3$					
C	4.2	4.2	10.73	24	3.03	−0.36	Black diamond

Notes. For the purpose of comparison with Lanz et al. (2016), we have assumed the area corresponding to each radial size, r, as $A = \pi r^2$. $M^{\rm enc}_{\rm H_2}$ is the assumed cold molecular gas mass enclosed within $r_{\rm H_2}$. SFR in units of $M_\odot$ yr^{-1}. $\Sigma_{\rm M_{H_2}}$ in $M_\odot$ pc^{-2}. $r_{\rm CO}$ = 358 pc is the CO(2–1) half light radius inferred with ALMA data (see text). $r_{\rm disk}$ = 2 kpc is the radius of the molecular disk discovered by Fotopoulou et al. (2019). Case C corresponds to Lanz et al. (2016). All molecular masses were calculated with $\alpha_{\rm CO}$ = 0.78, except in case C, for which $\alpha_{\rm CO}$ = 4.3 as in Lanz et al. (2016). The last column specifies the symbol used in Fig. 13.

We have considered different possible values for $r_{\rm H2}$. In case A (Table 5), $r_{\rm H2} = r_{\rm CO}$ and the mass within is $\log(M_{\rm H_2}/M_\odot) = 9.36$. This implies $\log(\Sigma_{\rm M_{H_2}}=3.76)$, that is within the range 2.59–4.49 (log of the median 3.91) in Pereira-Santaella et al. (2021; see also Bellocchi et al. 2022).

Based on CO(1–0), (3–2), and (4–3) line observations with ALMA, Fotopoulou et al. (2019) discovered that most of the total molecular gas of 4C12.50 is within $r \sim 2$ kpc (this is consistent with our CO(2–1) ALMA data), including a disk of radius $r_{\rm disk}$ = 2 kpc, associated with the western nucleus. Although they detected more extended molecular gas, its mass is relatively low. In case B, we thus assume $r_{\rm H_2}$ = 2 kpc and $\log(M_{\rm H_2}/M_\odot) = 10.00$, which is the total cold molecular gas of the system. For the sake of comparison with Lanz et al. (2016), we assume $r_{\rm SF} = r_{\rm H_2}$, although this $r_{\rm SF}$ is likely to be unrealistically large (see above).

Finally, we assume the values adopted by Lanz et al. (2016), $r_{\rm SF} = r_{\rm H_2}$ = 4.2 kpc (case C). This is the extent of the main CO(1–0) spatial component, which Dasyra et al. (2014) found to be marginally resolved within the beam size based on IRAM Plateau de Bure Interferometer data. These authors used $\alpha_{\rm CO}$ = 4.3 (K km^{-1} s^{-1} pc^2)$^{-1}$ (instead of 0.78), leading to a significantly higher total molecular gas mass of $\log(M_{\rm H_2}/M_\odot) = 10.73$.

$\Sigma_{\rm M_{H_2}}$ and $\Sigma_{\rm SFR}$ for cases A to C are shown in Table 5, and their locations on the K–S relation are shown in Fig. 13. As argued by Daddi et al. (2010a), this diagram suggests the existence of two different regimes of star formation: a long-lasting mode for disks, and a more rapid mode for starbursts (including U/LIRGs and sub-millimeter galaxies (SMG)), the latter probably occurring during major mergers or in dense nuclear star-forming regions. They considered the total neutral and molecular gas. We use only the cold molecular gas in 4C12.50, because the neutral gas mass in ULIRGs is in general negligible in comparison (Daddi et al. 2010b).

Being a ULIRG undergoing a major merger, we would expect 4C12.50 to lie near the starburst sequence. On the contrary, Lanz et al. (2016) found that the object is not only well below it, but well below the normal-disks sequence as well (see black diamond in Fig. 13).

Based on our revised location of 4C12.50 in the K-S diagram, we cannot confirm this conclusion. In fact, the location based on the new ALMA measurements (case A lower limits represented as triangles in the figure in Table 5), all lie close or above the starburst region. Given that $r_{\rm CO}$ is most probably a lower limit of $r_{\rm SF}$, we find no evidence for star formation suppression in this object. Positive feedback, in the sense of an enhancement of the star formation activity induced by the jet, may be present. To investigate this more accurate determinations of both the SFR and, specially, $r_{\rm SF}$ would be very valuable.

The main reason for the discrepancy with Lanz et al. (2016) is their assumption of unrealistically large $r_{\rm H2} \sim r_{\rm SF} \sim 4.2$ kpc. Another important difference is the lower SFR∼24 $M_\odot$ yr^{-1} and the assumed $\alpha_{\rm CO}$ = 4.3. While this conversion factor is appropriate for galaxies in the disk sequence, $\alpha_{\rm CO}$ = 0.78 is more appropriate for U/LIRGs. This difference was taken into account by Daddi et al. (2010a), who used $\alpha_{\rm CO}$ values adequate for each galaxy type.

5.3. No solid evidence for a significant impact of radio-induced feedback on the evolution of 4C12.50

Overall, there is no solid evidence for the radio jet to have a significant impact on the evolution of 4C12.50, not by clearing out the dusty central cocoon, nor by suppressing the star formation activity. It is possible that we are observing 4C12.50 in a very early phase of the radio activity. At the moment, the radio source appears to be affecting just a small volume. However, as times passes, unless its advance is frustrated by the rich gaseous medium, the jet will propagate through the galaxy and possibly expand beyond it at some point. Signs of a previous radio outburst stretching outside the host shows that this has happened in the past (Lister et al. 2003; Stanghellini et al. 2005). If the radio jet decelerates and inflates into large expanding bubbles, it will affect a much larger galactic volume. Whether it will carry enough energy to expel the cocoon and-or to prevent further gas cooling and-or to inject turbulence, affecting in this way future star formation is unknown (Mukherjee et al. 2016; Morganti et al. 2021).

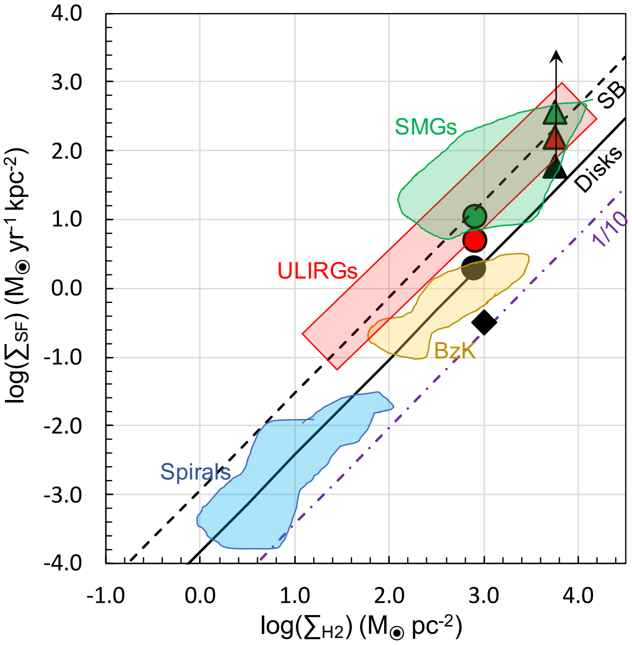

Fig. 13. Surface density of star formation compared to gas (cold molecular + neutral) density gas (K–S diagrams; Kennicutt 1998). This figure has been adapted from Fig. 2 in Daddi et al. (2010a). The coloured areas roughly enclose different galaxy types indicated with labels. The black solid line ('disks sequence') is a fit to local spirals and $z \sim 1.5$ BzK selected galaxies (slope of 1.42). The upper dashed line is the same relation shifted up by 0.9 dex to fit local U/LIRGs and SMGs. The dot-dashed purple line corresponds to a star formation suppression of a factor of 10 relative to the disks sequence. The coloured symbols are different locations of 4C12.50 for the diversity of parameters used in our calculations. The triangles correspond to cases A and the circles correspond to cases B in Table 5. The black diamond comes from Lanz et al. 2016 (case C). The triangles represent the values obtained from recent high angular resolution ALMA CO(2–1) data.

The presence of other feedback mechanisms acting on different spatial scales should not be forgotten (AGN and-or starburst driven-winds). Their action is suggested by Rupke et al. (2005) results. They detected blueshifted NaID absorption due to a neutral outflow in the western nucleus, with $V_{\rm max}$ = 364 km s^{-1}, $M \sim 8\times10^8$ $M_\odot$, $\dot{M}$ = 0.88 $M_\odot$ yr^{-1} and log($\dot{E}$(erg s^{-1}))∼41.16 or ∼0.001% of $L_{\rm bol}$ (but see Perna et al. 2021). They locate it up to a radius of ∼10–15 kpc, and at a large angle from the radio axis. Therefore, there is no clear link between this outflow and the radio source.

6. Summary and conclusions

We present for the first time a detailed analysis of the hot (>1500 K) molecular H$_2$ gas in the ultraluminous infrared radio galaxy 4C12.50 at z = 0.122 based on GTC EMIR and VLT X-shooter near-infrared long slit spectroscopy of the western primary nucleus. New results on the ionised (including coronal) phase are also presented.

– 4C12.50 hosts a large hot molecular gas content, with $M_{\rm H_2}^{\rm hot}$ = (2.10 ± 0.44) × 10^4 $M_\odot$. This is consistent with its high infrared luminosity and with the large mass of cold (≲25 K) molecular gas.

– An unusually high rotational temperature $T_{\rm rot}$ = 3020 ± 160 K is inferred for H$_2$. This is at the high end of values measured in galaxies in general.

– The molecular gas mass obeys a power-law temperature distribution $\frac{dM_{\rm H2}}{dT} \propto T^{-5}$ from $T \sim 300$ K and up to ∼3000 K. This is consistent with paraboloidal bow shock model predictions. This, and the high $T_{\rm rot}$, suggests that, as found by other authors for the warm H$_2$ MIR emission lines, shocks (probably induced by the radio jet) contribute to the heating and excitation of the hot molecular gas. The jet-induced shocks can heat the molecular gas, even it the dynamical coupling is weak.

– The H$_2$ 2–0 S(3)λ1.1175/2–1 S(3)λ2.0735 ratio implies an extinction of $E_{B-V}^{\rm mol}$ = 0.35 ± 0.08 for the hot molecular gas. For comparison, the extinction inferred by other authors for the integrated ionised gas emission is $E_{B-V}^{\rm ion}$ = 0.59 ± 0.11.

– We find no evidence for a hot molecular outflow in the NIR H$_2$ lines. The warm (∼400 K) H$_2$ outflow tentatively identified in the MIR lines by other authors should have been detected, if the relative flux contribution was the same. This is not the case.

– In spite of the dramatic impact of the radio jet-induced shocks on the dynamics of the ionised and neutral phases of 4C12.50, the dynamics of the hot molecular gas is not obviously affected. This is consistent with previous works that suggest the poor coupling of the outflowing ionised and neutral outflows with the molecular gas at lower temperatures.

– The extreme Paα kinematics are consistent with those of the optical lines, including several forbidden ones. The prominent broad blueshifted Paα excess is not produced by the broad line region. It is due to the kinematically extreme ionised outflow previously identified in the optical. The outflow dominates (81 ± 4%) the Paα flux.

– Most of (possibly all) the coronal gas appears to be outflowing, with blueshifted and very broad [SiVI]λ1.963 and [FeVII]λ6087 ($FWHM$ = 3430 ± 450 km s^{-1} and $\Delta V_{\rm sys}$ = −1350 ± 190 km s^{-1} for the broadest component of [SiVI]).

– The relative contribution of the most turbulent (broadest) outflowing gas component to the total forbidden line fluxes, $\frac{F_{\rm br}}{F_{\rm tot}}$, correlates with the critical density $n_{\rm crit}$ in log. This suggests that a single mechanism (the radio jet) is responsible for the outflow identified in all lines emitted by the ionised phase, from the coronal to the lowest ionisation.

– If the outflowing ionised gas moving away from the observer is completely extinguished, it could be truly kinematically extreme, with $FWHM$ ∼ 5400 km s^{-1} (∼7000 km s^{-1} for the coronal gas), only comparable to those seen in a handful of high z extremely luminous quasars. Its mass and energetics would still be moderate.

– Based on ALMA CO(2–1) data and a new estimation of the star formation rate, we revise the location of 4C12.50 in the K–S diagram. Contrary to other studies, we claim that there is no evidence for star formation suppression in this object. Positive feedback as a consequence of jet-induced star formation is not discarded.

If radio-induced feedback can regulate the star formation activity in galaxies, 4C12.50 is a promising candidate to reveal this phenomenon in action. The rich amount of knowledge available for this object, however, has not provided solid evidence so far for this to be the case. We find no solid evidence for current or past impact of this mechanism on the evolution of this system, neither by clearing out the dusty central cocoon efficiently, nor by suppressing the star formation activity.

Acknowledgements. We thank an anonymous referee for revising the paper and contributing with constructive comments. This research has made use of grants

PGC2018-094671-BI00, PID2021-124665NB-I00 (M.V.M., A.C. and A.A.H.) and PIB2021-127718NB-100 (L.C.) by the Spanish Ministry of Science and Innovation/State Agency of Research MCIN/AEI/ 10.13039/501100011033 and by 'ERDF A way of making Europe'. I.L. acknowledges support from the Spanish Ministry of Science and Innovation (MCIN) by means of the Recovery and Resilience Facility, and the Agencia Estatal de Investigación (AEI) under the projects with references BDC20221289 and PID2019-105423GA-I00. E.B. acknowledges the María Zambrano programme of the Spanish Ministerio de Universidades funded by the Next Generation European Union and is also partly supported by grant RTI2018-096188-B-I00 funded by MCIN/AEI/10.13039/501100011033. Based on observations carried out at the Observatorio Roque de los Muchachos (La Palma, Spain) with EMIR on GTC (programme GTC16-21B) and at the European Organisation for Astronomical Research in the Southern hemisphere with X-shooter on VLT (ESO programme 091.B-0256(A)). We thank the observatories staff for their support with the observations. It also makes use of the following ALMA data: ADS/JAO.ALMA#2018.1.00699.S. ALMA is a partnership of ESO (representing its member states), NSF (USA) and NINS (Japan), together with NRC (Canada) and NSC and ASIAA (Taiwan) and KASI (Republic of Korea), in cooperation with the Republic of Chile. The Joint ALMA Observatory is operated by ESO, AUI/NRAO and NAOJ. The National Radio Astronomy Observatory is a facility of the National Science Foundation operated under cooperative agreement by Associated Universities, Inc. This research has made use of: (1) the VizieR catalogue access tool, CDS, Strasbourg, France. The original description of the VizieR service was published in Ochsenbein et al. (2000); (2) the Cosmology calculator by Wright (2006); (3) the NASA/IPAC Extragalactic Database (NED), which is operated by the Jet Propulsion Laboratory, California Institute of Technology, under contract with the National Aeronautics and Space Administration; (4) data from Sloan Digital Sky Survey. Funding for the SDSS and SDSS-II has been provided by the Alfred P. Sloan Foundation, the Participating Institutions, the National Science Foundation, the U.S. Department of Energy, the National Aeronautics and Space Administration, the Japanese Monbukagakusho, the Max Planck Society, and the Higher Education Funding Council for England. The SDSS Web Site is `http://www.sdss.org/`.

References

Alonso-Herrero, A., Poulton, R., Roche, P. F., et al. 2016, MNRAS, 463, 2405
Álvarez-Márquez, J., Labiano, A., Guillard, P., et al. 2023, A&A, 672, A108
Batcheldor, D., Tadhunter, C., Holt, J., et al. 2007, ApJ, 661, 70
Bellocchi, E., Pereira-Santaella, M., Colina, L., et al. 2022, A&A, 664, A60
Bennert, N., Jungwiert, B., Komossa, S., et al. 2006, A&A, 456, 953
Bianchin, M., Riffel, R. A., Storchi-Bergmann, T., et al. 2021, MNRAS, 510, 639
Bridges, T. J., & Irwin, J. A. 1998, MNRAS, 300, 967
Caglar, T., Burtscher, L., Brandl, B., et al. 2020, A&A, 634, A114
Calzetti, D., Armus, L., Bohlin, R. C., et al. 2000, ApJ, 533, 682
Cerqueira-Campos, F. C., Rodríguez-Ardila, A., Riffel, R., et al. 2021, MNRAS, 500, 2666
Colina, L., Arribas, S., & Monreal-Ibero, A. 2005, ApJ, 621, 725
Colina, L., Piqueras López, J., Arribas, S., et al. 2015, A&A, 578, A48
Condon, J. J., Huang, Z.-P., Yin, Q. F., et al. 1991, ApJ, 378, 65
Cortzen, I., Garrett, J., Magdis, G., et al. 2019, MNRAS, 482, 1618
Daddi, E., Elbaz, D., Walter, F., et al. 2010a, ApJ, 714, L118
Daddi, E., Bournaud, F., Walter, F., et al. 2010b, ApJ, 713, 686
Dale, D. A., Sheth, K., Helou, G., et al. 2005, AJ, 129, 2197
Dasyra, K. M., & Combes, F. 2011, A&A, 533, L10
Dasyra, K. M., & Combes, F. 2012, A&A, 541, L7
Dasyra, K. M., Tacconi, L. J., Davies, R. I., et al. 2006, ApJ, 638, 745
Dasyra, K. M., Combes, F., Novak, G. S., et al. 2014, A&A, 565, A46
Davies, R. I., Sternberg, A., Lehnert, M., et al. 2003, ApJ, 597, 907
De Looze, I., Cormier, D., Lebouteiller, V., et al. 2014, A&A, 568, A62
De Robertis, M. M., & Osterbrock, D. E. 1984, ApJ, 286, 171
De Robertis, M. M., & Osterbrock, D. E. 1986, ApJ, 301, 727
den Brok, J. S., Koss, M. J., Trakhtenbrot, B., et al. 2022, ApJS, 261, 7
Díaz-Santos, T., Charmandaris, V., Armus, L., et al. 2010, ApJ, 723, 993
Emonts, B. H. C., Piqueras-López, J., Colina, L., et al. 2014, A&A, 572, A40
Emonts, B. H. C., Morganti, R., Villar-Martín, M., et al. 2016, A&A, 596, A19
Evans, A. S., Kim, D. C., Mazzarella, J. M., et al. 1999, ApJ, 521, L107
Evans, A. S., Mazzarella, J. M., Surace, J. A., et al. 2002, ApJ, 580, 749
Farrah, D., Efstathiou, A., Afonso, J., et al. 2022, MNRAS, 513, 4770
Fotopoulou, C. M., Dasyra, K. M., Combes, F., et al. 2019, A&A, 629, A30
Gilmore, G., & Shaw, M. A. 1986, Nature, 321, 750
Grandi, S. A. 1977, ApJ, 215, 446
Guillard, P., Ogle, P. M., Emonts, B. H. C., et al. 2012, ApJ, 747, 95
Girdhar, A., Harrison, C. M., Mainieri, V., et al. 2022, MNRAS, 512, 1608
Heckman, T. M., Smith, E. P., Baum, S. A., et al. 1986, ApJ, 311, 526
Holt, J., Tadhunter, C. N., & Morganti, R. 2003, MNRAS, 342, 227
Holt, J., Tadhunter, C. N., Morganti, R., et al. 2011, MNRAS, 410, 1527
Imanishi, M., Nakanishi, K., & Izumi, T. 2016, AJ, 152, 218
Imanishi, M., Nakanishi, K., & Izumi, T. 2018, ApJ, 856, 143
Jarvis, M. E., Harrison, C. M., Thomson, A. P., et al. 2019, MNRAS, 485, 2710
Kennicutt, R. C. 1998, ApJ, 498, 541
Lanz, L., Ogle, P. M., Alatalo, K., et al. 2016, ApJ, 826, 29
Lamperti, I., Koss, M., Trakhtenbrot, B., et al. 2017, MNRAS, 467, 540
Lamperti, I., Pereira-Santaella, M., Perna, M., et al. 2022, A&A, 668, A45
Larkin, J. E., Armus, L., Knop, R. A., et al. 1998, ApJS, 114, 59
Lister, M. L., Kellermann, K. I., Vermeulen, R. C., et al. 2003, ApJ, 584, 135
Machalski, J., Chyży, K. T., Stawarz, Ł., et al. 2007, A&A, 462, 43
Machalski, J., Jamrozy, M., & Saikia, D. J. 2009, MNRAS, 395, 812
Małek, K., Pollo, A., Takeuchi, T. T., et al. 2013, Earth Planets Space, 65, 1101
Mazzalay, X., Saglia, R. P., Erwin, P., et al. 2013, MNRAS, 428, 2389
Mezcua, M., Prieto, M. A., Fernández-Ontiveros, J. A., et al. 2015, MNRAS, 452, 4128
Mirabel, I. F. 1989, ApJ, 340, L13
Mirabel, I. F., Sanders, D. B., & Kazes, I. 1989, ApJ, 340, L9
Mittal, R., Oonk, J. B. R., Ferland, G. J., et al. 2012, MNRAS, 426, 2957
Morganti, R., Tadhunter, C. N., Oosterloo, T. A., et al. 2003, PASA, 20, 129
Morganti, R., Oosterloo, T. A., Tadhunter, C. N., et al. 2004, A&A, 424, 119
Morganti, R., Tadhunter, C. N., & Oosterloo, T. A. 2005, A&A, 444, L9
Morganti, R., Fogasy, J., Paragi, Z., et al. 2013, Science, 341, 1082
Morganti, R., Oosterloo, T., Tadhunter, C., et al. 2021, A&A, 656, A55
Mukherjee, D., Bicknell, G. V., Sutherland, R., et al. 2016, MNRAS, 461, 967
Müller Sánchez, F., Davies, R. I., Eisenhauer, F., et al. 2006, A&A, 454, 481
Murphy, T. W., Soifer, B. T., Matthews, K., et al. 2001, AJ, 121, 97
Neufeld, D. A., & Yuan, Y. 2008, ApJ, 678, 974
Ocaña Flaquer, B., Leon, S., Combes, F., et al. 2010, A&A, 518, A9
Ochsenbein, F., Bauer, P., & Marcout, J. 2000, A&AS, 143, 23
O'Dea, C. P. 1998, PASP, 110, 493
O'Dea, C. P., & Saikia, D. J. 2021, A&ARv, 29, 3
O'Dea, C. P., De Vries, W. H., Worrall, D. M., et al. 2000, AJ, 119, 478
Ogle, P., Boulanger, F., Guillard, P., et al. 2010, ApJ, 724, 1193
Oh, K., Koss, M., Markwardt, C. B., et al. 2018, ApJS, 235, 4
Osterbrock, D. E., & Ferland, G. J. 2006, Astrophysics of Gaseous Nebulae and Active Galactic Nuclei (University Science Books)
Pereira-Santaella, M., Spinoglio, L., van der Werf, P. P., et al. 2014, A&A, 566, A49
Pereira-Santaella, M., Colina, L., García-Burillo, S., et al. 2021, A&A, 651, A42
Perna, M., Arribas, S., Pereira Santaella, M., et al. 2021, A&A, 646, A101
Perrotta, S., Hamann, F., Zakamska, N. L., et al. 2019, MNRAS, 488, 4126
Piqueras López, J., Colina, L., Arribas, S., et al. 2012, A&A, 546, A64
Piqueras López, J., Colina, L., Arribas, S., et al. 2013, A&A, 553, A85
Ramos Almeida, C., García, Pérez, & A. M., Acosta-Pulido, J., 2009, ApJ, 694, 1379
Ramos Almeida, C., Acosta-Pulido, J. A., Tadhunter, C. N., et al. 2019, MNRAS, 487, L18
Ramos Almeida, C., Bischetti, M., García-Burillo, S., et al. 2022, A&A, 658, A155
Rich, J. A., Kewley, L. J., & Dopita, M. A. 2015, ApJS, 221, 28
Riffel, R., Rodríguez-Ardila, A., & Pastoriza, M. G. 2006, A&A, 457, 61
Riffel, R. A., Storchi-Bergmann, T., Riffel, R., et al. 2013, MNRAS, 429, 2587
Riffel, R. A., Vale, T. B., Storchi-Bergmann, T., et al. 2014, MNRAS, 442, 656
Riffel, R. A., Storchi-Bergmann, T., Riffel, R., et al. 2021, MNRAS, 504, 3265
Rodríguez-Ardila, A., Viegas, S. M., Pastoriza, M. G., et al. 2002, ApJ, 579, 214
Rodríguez-Ardila, A., Pastoriza, M. G., Viegas, S., et al. 2004, A&A, 425, 457
Rodríguez-Ardila, A., Riffel, R., & Pastoriza, M. G. 2005, MNRAS, 364, 1041
Rodríguez-Ardila, A., Prieto, M. A., Portilla, J. G., et al. 2011, ApJ, 743, 100
Rodríguez Zaurín, J., Tadhunter, C. N., Rose, M., et al. 2013, MNRAS, 432, 138
Rose, M., Tadhunter, C. N., Holt, J., et al. 2011, MNRAS, 414, 3360
Rose, M., Tadhunter, C., Ramos Almeida, C., et al. 2018, MNRAS, 474, 128
Rupke, D. S., Veilleux, S., & Sanders, D. B. 2005, ApJ, 632, 751
Sadler, E. M. 2016, Astron. Nachr., 337, 105
Santoro, F., Tadhunter, C., Baron, D., et al. 2020, A&A, 644, A54
Scoville, N. Z., Hall, D. N. B., Ridgway, S. T., et al. 1982, ApJ, 253, 136
Smolčić, V., & Riechers, D. A. 2011, ApJ, 730, 64
Soifer, B. T., Neugebauer, G., Matthews, K., et al. 2000, AJ, 119, 509
Solomon, P. M., & Vanden Bout, P. A. 2005, ARA&A, 43, 677

Speranza, G., Ramos Almeida, C., Acosta-Pulido, J. A., et al. 2022, A&A, 665, A55
Spoon, H. W. W., & Holt, J. 2009, ApJ, 702, L42
Spoon, H. W. W., Armus, L., Marshall, J. A., et al. 2009, ApJ, 693, 1223
Stanghellini, C., O'Dea, C. P., Dallacasa, D., et al. 2005, A&A, 443, 891
Tadhunter, C., Holt, J., González Delgado, R., et al. 2011, MNRAS, 412, 960
Tadhunter, C., Morganti, R., Rose, M., et al. 2014, Nature, 511, 440
Tadhunter, C., Rodríguez Zaurín, J., Rose, M., et al. 2018, MNRAS, 478, 1558
Togi, A., & Smith, J. D. T. 2016, ApJ, 830, 18
Vacca, W. D., Cushing, M. C., & Rayner, J. T. 2003, PASP, 115, 389
Veilleux, S., Sanders, D. B., & Kim, D.-C. 1997, ApJ, 484, 92
Veilleux, S., Rupke, D. S. N., Kim, D.-C., et al. 2009, ApJS, 182, 628
Villar-Martín, M., Rodríguez, M., Drouart, G., et al. 2013, MNRAS, 434, 978
Villar Martín, M., Bellocchi, E., Stern, J., et al. 2015, MNRAS, 454, 439
Villar Martín, M., Emonts, B., Cabrera Lavers, A., et al. 2017, MNRAS, 472, 4659
Villar Martín, M., Perna, M., Humphrey, A., et al. 2020, A&A, 634, A116
Villar Martín, M., Emonts, B. H. C., Cabrera Lavers, A., et al. 2021, A&A, 650, A84
Vivian, U., Sanders, D. B., Mazzarella, J. M., et al. 2012, ApJS, 203, 9
Wright, E. L. 2006, PASP, 118, 1711
Zakamska, N. L. 2010, Nature, 465, 60
Zakamska, N. L., Strauss, M. A., Krolik, J. H., et al. 2003, AJ, 126, 2125
Zhu, H., Tian, W., Li, A., et al. 2017, MNRAS, 471, 3494